Macrophage network dynamics depend on haptokinesis for optimal local surveillance

Neil Paterson [1, 2, 3], Tim Lämmermann [1, *]

Affiliations:

1 Max Planck Institute of Immunobiology and Epigenetics, Freiburg, 79108, Germany.

2 International Max Planck Research School for Immunobiology, Epigenetics and Metabolism (IMPRS-IEM), Freiburg, 79108, Germany.

3 Faculty of Biology, University of Freiburg, Freiburg, 79104, Germany.

* Corresponding author: laemmermann@ie-freiburg.mpg.de

Address:
Max Planck Institute of Immunobiology and Epigenetics
Stübeweg 51
79108 Freiburg
Germany
Phone: +49-761-5108-717

Key words:

macrophage, haptokinesis, leukocytes, cell networks, migration, integrins, cytoskeleton, tissue surveillance, tissue homeostasis, efferocytosis, sampling, mesenchymal movement, amoeboid cell shape

Summary

Macrophages are key immune cells with important roles for tissue surveillance in almost all mammalian organs. Cellular networks made up of many individual macrophages allow for optimal removal of dead cell material and pathogens in tissues. However, the critical determinants that underlie these population responses have not been systematically studied. Here, we investigated how cell shape and the motility of individual cells influences macrophage network responses in 3D culture settings and in mouse tissues. We show that surveying macrophage populations can tolerate lowered actomyosin contractility, but cannot easily compensate for a lack of integrin-mediated adhesion. Although integrins were dispensable for macrophage chemotactic responses, they were crucial to control cell movement and protrusiveness for optimal surveillance by a macrophage population. Our study reveals that β1 integrins are important for maintaining macrophage shape and network sampling efficiency in mammalian tissues, and sets macrophage motility strategies apart from the integrin-independent 3D migration modes of many other immune cell subsets.

Introduction

Macrophages are multifunctional immune cells that populate practically all tissues in the body where they play important roles in tissue homeostasis, organ development, inflammation, metabolic adaptation, tumor development and host defense against pathogens (Okabe & Medzhitov, 2016; Wood & Martin, 2017). As professional phagocytic cells, one of the major homeostatic functions of macrophages, in both invertebrates and vertebrates, is the removal of dead cell corpses and tissue debris (efferocytosis) (Cox et al., 2021; Wood & Martin, 2017). While the phases of corpse recognition (find-me), uptake (eat-me) and digestion (digest-me) are molecularly well described in the context of individually responding cells (Davidson & Wood, 2020b; Elliott & Ravichandran, 2016; Rothlin et al., 2021), much less is known about the role of group dynamics in this process. It is well established that macrophages distribute in numerous mammalian tissues to form large networks of many individual cells (Dawson et al., 2020; Freitas-Lopes et al., 2017; Gordon et al., 2014; Honda et al., 2020; Jain & Weninger, 2013; Nicolas-Avila et al., 2020; Stolp et al., 2020; Uderhardt et al., 2019). However, the population aspect of macrophage efferocytosis in tissues has so far only received little attention and the single cell parameters that critically determine the efferocytic capacity of a whole macrophage population are only poorly understood. In particular, it remains unclear how the cytoskeletal control of single-cell shape and movement influences the efferocytic capacity of mammalian macrophage networks.

Cell shape and cell motility are determined by the balanced interplay of three components: actin polymerization, actomyosin contraction and adhesion to the extracellular environment (Bodor et al., 2020). Leukocyte migration in three-dimensional (3D) interstitial spaces is considered flexible and adaptive, with many immune cells switching to alternate migration modes upon perturbations of any of these three components (Lämmermann & Sixt, 2009). Our current view on interstitial leukocyte motility is still largely influenced by studies with fast-migrating immune cells (dendritic cells, neutrophils, lymphocytes) that traffic between parenchyma and vasculature of mouse tissues (Lämmermann & Germain, 2014). Previous work on these cell types has highlighted that leukocyte motility outside the vasculature relies almost exclusively on cell shape changes driven by the actomyosin cytoskeleton (Lämmermann et al., 2013; Lämmermann et al., 2008; Woolf et al., 2007). This migration mode, commonly referred to as amoeboid migration, is independent from integrin adhesion receptors and strong adhesive interactions with the tissue environment (Paluch et al., 2016; Reversat et al., 2020). Macrophages, as archetypes of tissue-resident immune cells, appear to contrast most other leukocytes. Macrophages in zebrafish larvae (Barros-Becker et al., 2017) and human monocyte-derived macrophages invading into 3D matrigels (Van Goethem

et al., 2011; Van Goethem et al., 2010) move with elongated morphology at lower speeds and show adhesion structures containing heterodimeric integrin receptors (Hynes, 2002). This mode of locomotion is best described as a mesenchymal-like migration and rather resembles the movement patterns of fibroblasts and other non-immune cell types (Yamada & Sixt, 2019). Macrophages in mice also protrude elongated processes for tissue surveillance in almost all organs. Moreover, they are well known as very adhesive cell type with a broad range of different integrin adhesion receptors on their surface (Ley et al., 2016). However, we still have very limited knowledge on the functional contribution of integrins to macrophage shape, positioning and migration in 3D interstitial spaces of murine tissues. Studies of Drosophila macrophages, so-called hemocytes, provide currently the best insight into this question. Mutating the main βPS integrin in Drosophila causes hemocyte migration deficits in embryos (Comber et al., 2013) and late pupal stages (Moreira et al., 2013), but a direct comparison between Drosophila and mouse macrophages is problematic. Hemocytes move in highly confined, fluid-filled spaces, where only over time these macrophages together with other cells deposit extracellular matrix (Matsubayashi et al., 2017; Sanchez-Sanchez et al., 2017). Thus, it remains unclear how these findings relate to macrophage behavior in geometrically complex, often matrix-rich interstitial spaces of mammalian tissues. Here, we systematically address how lack of integrin functionality influences macrophage motility in mouse tissues and 3D *in vitro* matrices, and how these cells adapt to a loss of adhesiveness. As the central point of this study, we investigate how the cell shape and the motility mode of individual cells influence the efferocytic efficiency of macrophage networks, and how perturbations on the single cell level may be compensated in a sampling phagocyte population.

Results

Haptokinetic random motility of macrophages in 3D matrices

Macrophages distribute homogeneously as cellular networks in most mouse tissues, as exemplified by tissue-resident macrophages of the brain-surrounding dura mater (Figure 1A). Studying network dynamics and migration of slow-migrating macrophages by two-photon intravital microscopy (2P-IVM) is however challenging and often limited to only a few hours. To overcome this restriction, we established an *in vitro* platform for the microscopic observation of macrophage network dynamics over 24 h and longer (Figure 1B and Video S1). We used primary mouse bone marrow-derived macrophages (BMDMs) (Weischenfeldt & Porse, 2008; Zajd et al., 2020), which were embedded into 3D matrigel. By combining this system with video-based brightfield microscopy, we monitored migration dynamics in

macrophage populations over 24–30 h and found that individual cells moved with mesenchymal-like elongated shapes at average speeds of ~ 0.6 µm/min (Figures 1C–1E). Treatment of BMDMs with the F-actin-disrupting drug cytochalasin D, the Rho-associated kinase (ROCK) inhibitor Y27632 or the non-muscle myosin II inhibitor blebbistatin revealed an essential requirement of actin dynamics and an important role of actomyosin contraction for macrophage random migration (Figures 1C–1E, Figure 1 – figure supplement 1). Treatment of BMDMs with the Arp2/3 complex inhibitor CK-666 caused cell rounding and loss of prominent mesenchymal protrusions in the majority of macrophages (Video S2). This resulted in a significant reduction in the average speed, supporting an important role of dendritic actin filament networks for 3D macrophage random migration (Figure 1 – figure supplement 1 and Video S2). To address the functional role of integrin-mediated adhesion, the third component determining cell migration, for macrophage 3D motility, we used different mouse crosses to generate BMDMs without functional high-affinity integrins (*Tln1*$^{-/-}$) or without cell surface integrin heterodimers of the β2 family (*Itgb2*$^{-/-}$) or β1 family (*Itgb1*$^{-/-}$) (Figure 1 – figure supplements 2 and 3). *Tln1*$^{-/-}$ BMDMs, which are depleted of talin, a crucial interactor with integrin cytoplasmic domains for integrin activation (Calderwood & Ginsberg, 2003), showed roundish, amoeboid-like morphologies and severely impaired random migration (Figures 1F–1I and Video S2). Confocal fluorescence microscopy of Lifeact-GFP expressing BMDMs in 3D matrices clearly revealed that *Tln1*$^{-/-}$ cells were missing the prominent branched protrusions that gave WT macrophages their mesenchymal-like cell shape (Figure 1K). *Itgb2*$^{-/-}$ BMDMs lack β2 integrins on the cell surface, including the strongly expressed heterodimer αMβ2 (Mac-1), a characteristic macrophage cell surface protein with promiscuous binding properties to more than 30 non-protein and protein molecules, including several ECM components (Yakubenko et al., 2002) (Figure 1 – figure supplement 3). Surprisingly, ITGB2-deficiency did not result in cell shape changes or migration deficiencies (Figures 1F–1I). However, *Itgb1*$^{-/-}$ BMDMs that lack the important extracellular matrix (ECM)-binding heterodimers α5β1 and α6β1 on their cell surface, copied the morphology and migration phenotype of *Tln1*$^{-/-}$ BMDMs (Figures 1F–1I; Figure 1 – figure supplement 3). Thus, our results identify a crucial role of β1 integrins for the mesenchymal-like movement of macrophages, highlighting the substrate-dependent (haptokinetic) nature of 3D macrophage random migration. Loss of integrin functionality and the associated switch from mesenchymal-like to amoeboid morphology results in severely impaired 3D motility, which macrophages cannot compensate in contrast to many other immune cell types.

β1 integrins determine the mesenchymal-like shape of macrophages in mouse tissues

To corroborate the importance of our *in vitro* findings for living tissues, we investigated tissue-resident macrophages of mice with conditional *Itgb1* deletion in hematopoietic cells.

This genetic approach allowed the efficient depletion of ITGB1 in hematopoietic stem cells and thus targeted also endogenous macrophages of different organs and ontogeny. Other genetic strategies (e.g. *Lyz2*^{CRE}, *Cx3cr1*^{CRE}) resulted in partial targeting of macrophage subsets or incomplete protein depletion, which did not provide conclusive *in vivo* results (data not shown). When we analyzed endogenous macrophage networks in several ECM-rich tissues by immunofluorescence analysis, the comparison of *Vav-iCre Itgb1*$^{fl/fl}$ mice with littermate controls provided a clear morphological phenotype. In agreement with our findings from 3D matrigels, ITGB1 depletion caused macrophages in the interstitial spaces of the skin dermis (Figure 2A), the splenic red pulp (Figure 2B) and in the sinusoidal spaces of the liver (Figure 2C) to adopt a roundish, amoeboid-like cell shape. In contrast, macrophages in tissues of *Itgb2*$^{-/-}$ mice retained their mesenchymal-like morphologies (Figure 2 – figure supplement 1). Thus, our results confirm the crucial role of β1 integrins for defining the mesenchymal-like shape of endogenous macrophages in several mouse tissues.

Integrin-independent macrophage movement during chemotactic responses

As external guidance signals can induce cell polarization and directed migration, we next examined the chemotactic migration response of macrophages. We embedded BMDMs in 3D matrigel scaffolds and followed their directed migration along a gradient of the chemoattractant complement factor 5a (C5a) over 24 h (Figure 3A). We then assessed the contribution of actin dynamics, actomyosin contraction and integrin function to this process (Figures 3B and 3C; Figure 3 – figure supplement 1). The effects of cytochalasin D and Y27632 treatment on chemotactic macrophage migration were comparable to our previous results on random motility (Figures 1C–1E), showing an essential requirement for actin dynamics and an important role for actomyosin contraction (Figures 3B, 3D and 3E). CK-666 treatment did not impair BMDM chemotaxis in 3D matrigel (Figure 3 – figure supplement 1), which is in agreement with previous studies showing that Arp2/3 complex blockade rather increases than decreases migration speed in several cell types (Asokan et al., 2014; Dimchev et al., 2021; Georgantzoglou et al., 2021; Leithner et al., 2016; Moreau et al., 2015; Rotty et al., 2017; Vargas et al., 2016; Wu et al., 2012). Strikingly, the dependency on integrin function was markedly different between random and chemotactic macrophage migration. In contrast to random motility, *Tln1*$^{-/-}$ and *Itgb1*$^{-/-}$ BMDMs, which had adopted more roundish and amoeboid-like shapes, moved at comparable average speeds to WT and *Itgb2*$^{-/-}$ BMDMs, which migrated with very elongated and mesenchymal-like morphologies along the C5a gradient (Figures 3C, 3F, 3G and Video S3). Track straightness and cell surface expression of C5aR1 were comparable between all gene variants (Figure 3 – figure supplement 2). Y27632 treatment impaired the chemotactic migration of *Tln1*$^{-/-}$ BMDMs, supporting an important role of actomyosin contractility as amoeboid protrusive force for

integrin-independent macrophage migration (Figure 3 – figure supplement 2). Thus, chemotactic guidance cues can overcome the migration deficit of adhesion-deficient macrophages and induce productive amoeboid-like, integrin-independent macrophage movement.

Amoeboid-like macrophages still perform chemotactic migration in mouse tissue

To confirm our findings *in vivo*, we chose to investigate the chemotactic response of tissue-resident macrophages to laser-induced wounds in the mouse dermis (Figure 4A). Previous intravital imaging studies in mice demonstrated wound attractants to induce chemotactic responses of several myeloid cell types, mostly neutrophils and tissue-resident macrophages (Lämmermann et al., 2013; Uderhardt et al., 2019). We crossed *Vav-iCre Itgb1*$^{fl/fl}$ mice with lysozyme M-GFP (*Lyz2*^{GFP}) knock-in reporter mice to visualize dermal myeloid cells by two-photon intravital microscopy (2P-IVM). In agreement with our immunofluorescence analysis of ear skin whole mount tissues (Figure 2A), 2P-IVM of GFP-positive macrophages in the unchallenged ear dermis confirmed that most ITGB1-deficient macrophages lacked the typical multi-protrusive mesenchymal-like phenotype of WT macrophages (Figure 4 – figure supplement 1). As neutrophils can influence macrophage dynamics at the wound site, we removed them from the blood circulation by administering Anti-Ly6G neutrophil-depleting antibodies. This experimental strategy allowed us to accurately analyze the functional contribution of β1 integrins in the chemotactic wound response of tissue-resident macrophages (Figure 4A). In contrast to our *in vitro* imaging over a whole day, 2P-IVM was limited to 90–120 minutes. Imaging WT macrophages at high magnification revealed that these cells quickly formed long protrusions toward the tissue lesion, while most cell bodies remained immotile during this short observation period (Figure 4B and Video S4). Although most *Itgb1*$^{-/-}$ macrophages displayed rounded morphologies in unchallenged skin, these cells also formed directed protrusions towards the damage site at comparable speeds to WT cells (Figures 4C, 4D and Video S4). We observed for *Itgb1*$^{-/-}$ macrophages a two-fold increase in cell body displacement (53 % of all analyzed *Itgb1*$^{-/-}$ cells, N=55) in comparison to WT macrophages (24 % of all analyzed WT cells, N=34), which we interpret as a switch to a more amoeboid migration mode (Figure 4E; Figure 4 – figure supplement 2 and Video S4). Thus, our *in vivo* results confirm the dispensable role of integrins for the chemotactic response of macrophages. They also show that chemotactic cues are sufficient to polarize the macrophage cytoskeleton and support directed integrin-independent 3D protrusive movement. These findings expand our previous results on the chemotactic behavior of fast-migrating immune cells (dendritic cells, neutrophils, B cells) (Lämmermann et al., 2008) to a slower migrating tissue-resident immune cell type.

Two efficient surveillance strategies for macrophage networks

Next, we investigated how cell shape changes and motility modes of individual macrophages influence the surveillance behavior of a whole macrophage network. To address this question, we adapted our 3D *in vitro* platform and added fluorescent beads with attached phosphatidylserine (PS) to macrophage populations in matrigel (Figure 5A). PS on the bead surface acted as an "eat-me" signal for macrophages (Segawa & Nagata, 2015), and a network of 400–500 macrophages was able to almost completely clear gels of a corresponding number of extracellular particles within 24 h (Figure 5B). Several hours after ingestion by macrophages, bead fluorescence was quenched due to the acidic environment of the phagolysosomal system, which could be measured as overall reduction in fluorescence (Figure 5 – figure supplement 1). Using this system, we set out to understand the cytoskeletal requirements of sampling macrophage populations. Cytochalasin D treatment served as negative control for our analysis, as the complete stalling of migration and protrusion formation inhibited macrophage space exploration and bead uptake over 24 h (Figures 5C–5E). In contrast, lowering actomyosin contractility by Y27632 treatment did not impact the sampling efficiency of a macrophage population (Figures 5C–5E). Although individual BMDMs moved under these conditions at only ~ 30 % of their normal speed (Figures 1D–1E), their gain in single cell protrusiveness compensated for this reduction in speed and allowed Y27632-treated macrophage populations equal space exploration and bead uptake as control populations (Figures 5C and 5F; Figure 5 – figure supplement 2). Thus, macrophage networks can use two equally efficient surveillance strategies: (a) surveillance by migration (Figure 5G and Video S5), and (b) surveillance by low-motile protrusion extension (Figure 5H and Video S5). Considering the broad heterogeneity of macrophages in mammalian tissues (Bleriot et al., 2020), this finding is very relevant and highlights that efficient tissue surveillance can be realized by macrophage subsets with migratory potential, but also by macrophage subsets with sessile, but protrusive behaviors.

Haptokinesis is required for optimal bead removal by macrophage networks

We then investigated how integrin-dependent haptokinesis influences the sampling efficiency of macrophage networks. We found that integrin-dependent deficits in macrophage random motility (Figures 1F–1I) translated directly to impaired removal of extracellular particles in matrigel (Figures 6A–C). Although *Tln1*$^{-/-}$ and *Itgb1*$^{-/-}$ BMDMs had comparable phagocytic activity to WT controls when macrophages were kept as cell suspensions during the incubation with PS-attached beads (Figure 6 – figure supplement 2), these mutant BMDMs showed clearly reduced bead internalization in the 3D matrix (Figures 6B and 6C; Figure 6 – figure supplement 1). Impaired haptokinesis of amoeboid-shaped *Tln1*$^{-/-}$ and *Itgb1*$^{-/-}$ BMDMs impeded efficient space exploration and bead sampling, which was not observed for

mesenchymal-like migrating *Itgb2*$^{-/-}$ BMDMs (Figures 6A–C; Figure 6 – figure supplement 1). Live cell imaging analysis revealed that the rudimentary movement of *Itgb1*$^{-/-}$ BMDMs was sufficient to sample beads in close vicinity to them, but the restricted movement radius prevented bead sampling of larger areas (Figure 6D and Video S6). However, we could rescue this surveillance deficit of *Itgb1*$^{-/-}$ BMDM networks by doubling the cell number in the macrophage population (Figures 6E and 6F). This result appears particularly relevant for physiological mammalian tissues, where the additional recruitment of monocytic cells or macrophages might compensate for insufficient space exploration of a tissue-resident macrophage network.

Haptokinesis is required for optimal efferocytosis by macrophage networks

The removal of dead cell material is best described as a sequential series of cell biological events divided into “find-me”, “eat-me” and “digest-me” phases (Lemke, 2019). To realize “eat-me”, individual macrophages are considered to chemotactically respond to “find-me” signals released from dead cells, a process that involves the formation of directed protrusions and subsequent cell displacement. However, it still remains unresolved which mechanisms guide and coordinate the dynamics of individual cells in macrophage networks where many phagocytes act together, but also compete for dead cell material. Given our disparate findings on integrin-dependent random motility and integrin-independent chemotactic responses of macrophages, we were particularly interested how loss of integrin functionality influences the sampling dynamics of macrophage networks. To study the efferocytosis response of macrophage populations, we added aged, fluorescently labeled mouse neutrophils to BMDM networks (Figure 7A). Aged neutrophils underwent cell death over time, and we used pHrodo-Red as fluorescent dye to label them. Efferocytosis was extremely efficient and a network of 300–400 macrophages was able to remove 500–700 dead neutrophils within 24–30 h (Figure 7B and Video S7). We observed that pHrodo fluorescence after the reported increase shortly after ingestion vanished inside macrophages several hours after neutrophil uptake, probably due to digestion of the corpse. We used this to measure the efferocytosis efficiency of BMDM networks as fluorescence decline, which we quantified by using two independent analysis programs (Figure 7C; Figure 7 – figure supplement 1). Microscopic observation of individual WT BMDMs revealed a spectrum of mesenchymal-like movement behaviors that supported efficient efferocytosis, including individual macrophages that sequentially ingested 8–14 cells over 24–30 h (Figure 7 – figure supplement 2 and Video S8). Testing the efferocytic capacity of integrin-deficient BMDM networks, we made again the striking observation that β1 integrin-dependent haptokinesis was crucial for optimal surveillance. As observed for the sampling of PS-attached beads that do not release “find-me” signals, networks of *Tln1*$^{-/-}$ and *Itgb1*$^{-/-}$ BMDMs were significantly

impaired in the removal of dead neutrophils. The phenotype of *Tln1*$^{-/-}$ BMDMs was even more pronounced in comparison to *Itgb1*$^{-/-}$ BMDMs, probably due to migration-independent effects of talin on αv integrins, which contribute to dead cell recognition and uptake (Lemke, 2019). In contrast, *Itgb2*$^{-/-}$ BMDMs showed similar efferocytic activities as WT cells (Figures 7C and 7D; Figure 7 – figure supplement 1). Haptokinetic movement of mesenchymal-shaped WT BMDMs at speeds of ~ 0.6 µm/min supported efficient sampling of corpses and surveillance of large areas (Figure 7E and Video S9), whereas impaired haptokinesis of *Itgb1*$^{-/-}$ BMDMs restricted surveillance to smaller regions (Figure 7F and Video S9). Although individual *Itgb1*$^{-/-}$ macrophages could ingest several dead neutrophils, the slow amoeboid-like movement limited their efferocytic sampling to only nearby corpses (Figure 7 – figure supplement 3). Thus, our results show an important role for β1 integrins in controlling macrophage movement and protrusiveness, and further highlight haptokinetic sampling as a crucial process for efficient efferocytosis in macrophage networks.

β1 integrin-dependent surveillance by cortical macrophage networks in lymph nodes

To show the relevance of our *in vitro* findings for mammalian tissues, we chose to study macrophages located in the T cell cortex of mouse lymph nodes (Figure 8A). These cortical macrophages sit on an ECM-rich reticular fiber scaffold, where they form dense cellular networks (Bellomo et al., 2018). Previous work has shown that this tissue-resident macrophage type acts as the only professional phagocyte that continuously clears apoptotic cells in the T cell zone of lymph nodes (Baratin et al., 2017). Confocal immunofluorescence analysis revealed dense networks of cortical macrophages with elongated protrusions and multi-branched, mesenchymal-like shapes in the T cell zones of WT mice (Figure 8B). In contrast, cortical macrophages in lymph nodes of conditional *Itgb1* knockout mice were more roundish and showed amoeboid-like morphologies (Figure 8B). To evaluate the efferocytic efficiency of cortical macrophage networks, we used the TUNEL method to detect and quantify apoptotic cells in the T cell zones of lymph nodes. TUNEL-positive cells were mostly detected inside cortical macrophages, but were also observed at lower numbers outside the macrophage network (Figure 8C). Importantly, mice with *Itgb1*-deficient macrophages showed a significantly increased number of extracellular, non-internalized apoptotic cells in T cell zones in comparison to littermate control mice (Figure 8D). Thus, our results confirm the important role of β1 integrin-dependent mesenchymal-like cell shape and motility for efferocytic macrophage networks *in vivo*.

Discussion

Given their many important physiological roles, macrophages have evolved mechanisms that ensure robust phago- and efferocytosis. Recent work in Drosophila embryos have strengthened this view by showing that hemocytes utilize two distinct modes of engulfment, “lamellipodial” and “filopodial” phagocytosis, which provide individual cells phagocytic plasticity to fulfill their clearance functions (Davidson & Wood, 2020a). Similar to this previous study, the removal of microbes and dead cells by macrophages has mostly been studied from the viewpoint of a single cell, trying to understand the molecular details of foreign material recognition and uptake (Elliott & Ravichandran, 2016; Mylvaganam et al., 2021; Vorselen et al., 2020). However, mammalian macrophages form cellular networks in almost all tissues, making tissue surveillance a “group effort” of many individual macrophages. This population behavior is important for the removal of dead cell material in tissues, where the efficiency of detecting, engulfing and clearing dead cell corpses depends on the efferocytic capacity of a whole macrophage population, which sometimes even requires additional support from non-professional phagocytes (Damisah et al., 2020; Han et al., 2016). Hence, it is evident that molecules recognizing “find-me” and “eat-me” signals and their surface expression levels on individual cells are important determinants for the efferocytic capacity of macrophage populations (Hughes et al., 2021; Rothlin & Ghosh, 2020).

Here, we investigated how the cell shape and the motility mode of individual macrophages influence the efferocytic capacity of macrophage networks. Our study sought to determine the critical and non-critical parameters that shape the dynamic surveillance behavior of macrophage networks in 3D environments. In particular, we focused on the cytoskeletal control of macrophage motility and migration, the basic processes that enable the formation of directed cell protrusions and displacement and thus realize the interstitial recruitment preceding the engulfment of dead cell corpses. Our findings expand the concept of plasticity to modes of tissue surveillance in macrophage networks. We show that actomyosin contractility is non-critical for sampling macrophage populations, as they can survey their surrounding by two equally efficient strategies: (a) surveillance by migration, or (b) surveillance by low-motile protrusion extension. We speculate that both surveillance modes are likely reflected in the heterogeneity of resident macrophages in mammalian tissues (Bleriot et al., 2020; Cox et al., 2021), contributing to the robustness of macrophage network function. Although we know that macrophages of different developmental origin co-exist in many tissues (Bleriot et al., 2020; Cox et al., 2021), we have only limited understanding about their cytoskeletal properties. In future studies it will be interesting to address how distinct macrophage subsets differ in their protrusive and contractile forces and how these

factors determine the surveillance potential and adaptation of macrophages to a specific tissue compartment (Okabe & Medzhitov, 2016).

As the most important result of our study, we identify that both surveillance strategies critically depend on haptokinesis. Integrin β1-mediated substrate binding controls the 3D mesenchymal-like shape, movement, lamellopodial protrusiveness and space exploration of individual cells in a sampling macrophage network. Loss of β1 integrin function switches the cells to an amoeboid-like morphology, which does not support random motility and the sampling of particles or dead cells by the macrophage network. In contrast to many other immune cell types (Lämmermann & Germain, 2014), we find that randomly migrating mouse macrophages cannot compensate for the loss of integrin function and the associated switch from a mesenchymal–to an amoeboid-like morphology. Previous studies with zebrafish macrophages and human monocyte-derived macrophages (hMDMs) in 3D matrix gels detected integrin-dependent adhesion structures (Barros-Becker et al., 2017; Van Goethem et al., 2011), but the functional consequences of integrin depletion for migration remained unexplored. Similar to immature dendritic cells (Gawden-Bone et al., 2014), mammalian macrophages form integrin-dependent focal adhesions and podosomes on 2D surfaces (Owen et al., 2007; Wiesner et al., 2014). Interestingly, studies with hMDMs invading 3D collagen gels found classical focal adhesion and podosome components (e.g. talin, paxillin, vinculin) at the tip of F-actin-rich cell protrusions together with β1 integrins (Van Goethem et al., 2011; Wiesner et al., 2014). However, the exact nature of the integrin-dependent adhesion structure promoting macrophage 3D migration remains to be explored in future studies.

To our surprise, we find contrasting integrin demands of random and chemotactic macrophage migration. When talin- or β1 integrin-deficient macrophages were exposed to gradients of high C5a attractant concentrations, these amoeboid-shaped cells polarized their leading edges toward the attractant source and moved chemotactically with speeds similar to control cells. This behavior is reminiscent of integrin-independent 3D chemotaxis of dendritic cells and neutrophils (Lämmermann et al., 2008), but at six- to sixteen-fold lower average speeds, respectively. Studies in Drosophila had shown varying results on integrin-dependence for the directed migration of hemocytes toward laser-induced tissue injuries (Comber et al., 2013; Moreira et al., 2013). Our 2P-IVM experiments on mouse skin confirmed that dermal macrophages do not require β1 integrins during their chemotactic response toward local gradients of wound attractants. Thus, strong chemotactic signals can induce and maintain the polarization of the macrophage actomyosin cytoskeleton, enabling productive migration in the absence of integrin-dependent substrate binding.

Our experiments also touched on the role of Arp2/3 complex-mediated formation of branched actin networks and their functional role for 3D macrophage migration. Arp2/3 activity is crucial for dendritic actin nucleation underneath the plasma membrane, controlling protrusive lamellipodia at the cell edge and thus the mesenchymal phenotype of many cell types (Rotty et al., 2013). Moreover, this protein complex is also involved in several other cellular processes, including phagocytosis (Jaumouille & Waterman, 2020; Papalazarou & Machesky, 2021). Similar to integrins, we find contrasting demands of Arp2/3 activity for random versus chemotactic 3D migration. Randomly migrating macrophages lost their mesenchymal phenotype upon CK-666 treatment and were impaired in their speed and displacement. Previous studies with macrophages and fibroblasts had already shown that defective Arp2/3 function resulted in loss of lamellipodia and altered the migration phenotype (Rotty et al., 2017; Suraneni et al., 2012; Swaney & Li, 2016; Wu et al., 2012). *Arpc2*-deficient BMDMs were found to move with increased speed over ECM-coated 2D surfaces (Rotty et al., 2017), in an experimental setup where the promiscuous binding of β2 integrins to cell culture ware influences the macrophage migration phenotype. In contrast, macrophage movement in 3D matrigels strictly depends on β1 integrin-mediated mechanotransduction, causing a substantial migration defect upon Arp2/3 complex inhibition. Yet, movement of CK-666 treated macrophages along a strong chemotactic gradient was unimpaired, which is in agreement with several previous studies on fibroblasts (Asokan et al., 2014; Dimchev et al., 2021; Wu et al., 2012), BMDMs (Rotty et al., 2017) and other immune cell types (Georgantzoglou et al., 2021; Leithner et al., 2016; Moreau et al., 2015; Vargas et al., 2016), supporting the general notion that dendritic actin networks rather inhibit than support persistent movement along chemotactic cues and in confined environments. As seen for low-adhesive neutrophils and dendritic cells (Georgantzoglou et al., 2021; Leithner et al., 2016), macrophages also rely on Arp2/3-mediated front actin networks for space exploration in complex environments. However, macrophages strictly depend on integrin-mediated ECM interactions to establish lamellopodial protrusions as exploratory structures. Their directed movement towards strong chemotactic gradients does not require integrins or Arp2/3, which is reminiscent of cell types that perform amoeboid migration, where persistent locomotion depends on actin flow and actomyosin contraction (Georgantzoglou et al., 2021; Leithner et al., 2016).

When macrophages survey their surrounding for dead cells, they are considered to sense attractants released from dying cells, so called “find-me” signals, which initiate the formation of directed protrusions and cell displacement toward the dead cell material (Elliott & Ravichandran, 2016; Lemke, 2019; Rothlin et al., 2021). Although we showed that integrin receptors were dispensable for 3D macrophage chemotaxis, integrin-mediated movement

and protrusiveness was absolutely critical for efferocytosis by a surveying macrophage network. We speculate that individual dying cells release only low amounts of attractants, which generate chemotactic signals that are too weak and transient to support the full polarization of the macrophage cytoskeleton in the absence of functional integrins. Thus, integrin-dependent stabilization of the mesenchymal-like cell shape is crucial for efficient efferocytosis by macrophage networks. Insufficient haptokinetic sampling compromises the efferocytic activity of macrophage networks, as shown for β1 integrin-deficient lymph node cortical macrophages whose clearance of apoptotic T cells was impaired.

Our results are particularly relevant for ECM-rich tissues where β1 integrins define the mesenchymal-like shape of endogenous macrophages. Macrophages in the skin dermis and dura mater interact with fibrillar interstitial matrix and basement membranes (BMs), splenic red pulp and lymph node cortical macrophages locate on top of BM-rich reticular fiber networks, and intravascular Kupffer cells align along the BMs of liver sinusoids. In all these examples, other integrin family members or adhesion receptor systems could not compensate the loss of β1 integrins and restore the mesenchymal-like shape of endogenous macrophages. β2 integrins, which are abundantly expressed on macrophages, appear not to be involved in pro-migratory mechanotransduction in these interstitial environments, and likely serve other macrophage functions (e.g. pattern recognition, complement- and IgG-mediated phagocytosis, cell retention) (Cui et al., 2018; Jaumouille et al., 2019; Torres-Gomez et al., 2020). αV integrins, which we did not target in this study, may also rather support other macrophage functions (e.g., apoptotic cell uptake, TGFβ activation) (Kelly et al., 2018; Lemke, 2019). For organs and tissue compartments with largely cellular composition (e.g., brain, glands, epithelial layers), the maintenance of the mesenchymal-like macrophage phenotype may not necessarily require integrin-dependent ECM binding (Brand et al., 2020; Meller et al., 2017). Instead, haptokinesis for efficient macrophage surveillance might be realized by other adhesion receptor systems, whose identification requires more systematic studies for many of these tissues.

In summary, our study highlights macrophages as a tissue-resident immune cell type that does not follow the general prevailing paradigm of integrin-independent 3D migration of immune cells. Substrate-dependent movement and protrusiveness are critical determinants for space exploration and efficient sampling of macrophage networks. Thus, integrins are not only critical for the migratory processes of intravascular crawling (Neupane et al., 2020), extravasation (Nourshargh et al., 2010) and invasion (Arasa et al., 2021), but also crucial for the interstitial movement of myeloid immune cell subsets. Our mechanistic insights will also

likely be relevant for other tissue-resident immune cell types, which have not yet been studied in detail.

Materials and Methods

Key resources table

REAGENT TYPE or RESOURCE	DESIGNATION	SOURCE	IDENTIFIER or REFERENCE
Antibody	Armenian Hamster Anti-CD61 (Integrin beta 3) PE-conjugated	BD Biosciences	Cat# 553347; RRID: AB_394800
Antibody	Armenian Hamster Anti-CD29 (Integrin beta 1) PE-conjugated	BioLegend	Cat# 102208; RRID: AB_312885
Antibody	Armenian Hamster IgG Isotype Control PE-conjugated	BioLegend	Cat# 400907; RRID: AB_326593
Antibody	Donkey anti-goat Alexa Fluor 488-conjugated	Thermo Fisher Scientific	Cat# A11055; RRID: AB_2534102
Antibody	Donkey anti-rabbit Alexa Fluor 568-conjugated	Thermo Fisher Scientific	Cat# A10042; RRID: AB_2534017
Antibody	Goat Anti-GFP Dylight™ 488-conjugated	Rockland	Cat# 600-141-215; RRID: AB_1961516
Antibody	Goat Anti-rabbit Alexa Fluor 405-conjugated	Thermo Fisher Scientific	Cat# A-31556; RRID: AB_221605
Antibody	Goat Anti-rabbit Alexa Fluor 700-conjugated	Thermo Fisher Scientific	Cat# A21038 RRID: AB_10373851
Antibody	Goat Anti-collagen IV	Merck Millipore	Cat# AB769 RRID: AB_92262
Antibody	Mouse Anti-talin	Sigma-Aldrich	Cat# T3287 RRID: AB_477572
Antibody	Rabbit Anti-actin	Sigma-Aldrich	Cat# A2066; RRID: AB_476693
Antibody	Rabbit Anti-collagen IV	Abcam	Cat# ab19808; RRID:AB_445160
Antibody	Rabbit Anti-Iba1	Wako	Cat# 019-19741; RRID: AB_839504
Antibody	Rabbit Anti-LYVE1	Abcam	Cat# AB14917 RRID: AB_301509
Antibody	Rabbit Anti-mouse HRP-conjugated	Agilent Dako	Cat# P0161; RRID: AB_2687969
Antibody	Rat Anti-CD11b (Integrin alpha M) PE-conjugated	BD Biosciences	Cat# 557397; RRID: AB_396680
Antibody	Rat Anti-CD16/CD32 Antibody	BD Biosciences	Cat# 553142; RRID: AB_394657
Antibody	Rat Anti-CD18 (Integrin beta 2) PE-conjugated	BD Biosciences	Cat# 553293; RRID: AB_394762
Antibody	Rat Anti-CD49d (Integrin alpha 4) PE-conjugated	Thermo Fisher Scientific	Cat# 12-0492-82; RRID: AB_465697
Antibody	Rat Anti-CD49e (Integrin alpha 5) PE-conjugated	BD Bioscience	Cat# 557447 RRID: AB_396710
Antibody	Rat Anti-CD49f (Integrin alpha 6) Alexa Fluor 488-conjugated	BioLegend	Cat# 313608; RRID: AB_493635
Antibody	Rat Anti-CD45R/B220 Brilliant violet 421-conjugated	BD Bioscience	Cat# 562922 RRID: AB_2737894
Antibody	Rat Anti-CD51 (Integrin alpha V) PE-conjugated	BD Biosciences	Cat# 551187; RRID: AB_394088
Antibody	Rat Anti-CD68 Alexa Flour 488-conjugated	Biolegend	Cat#137011 RRID: AB_2074847
Antibody	Rat Anti-CD206 PE-Dazzle™	Biolegend	Cat#141731 RRID: AB_2565931
Antibody	Rat Anti-F4/80 Brilliant violet 421-conjugated	Biolegend	Cat# 123137 RRID: AB_2563102
Antibody	Rat Anti-F4/80 PE-conjugated	Thermo Fisher Scientific	Cat# MF48004; RRID: AB_10372666
Antibody	Rat Anti-F4/80 Alexa Flour 647-conjugated	Thermo Fisher Scientific	Cat# 50-4801-82 RRID: AB_11149361
Antibody	Rat Anti-Integrin β7 Chain PE-conjugated	BD Biosciences	Cat# 557498; RRID: AB_396735

Antibody	Rat IgG1 kappa Isotype Control PE-conjugated	Thermo Fisher Scientific	Cat# 12-4301-81; RRID: AB_470046
Antibody	Rat IgG2a Isotype Control Alexa Fluor 488-conjugated	Thermo Fisher Scientific	Cat# R2a20; RRID: AB_2556535
Antibody	Rat IgG2a kappa Isotype Control PE-conjugated	Thermo Fisher Scientific	Cat# 12-4321-80; RRID: AB_1834380
Antibody	Rat IgG2b kappa Isotype Control PE-conjugated	Thermo Fisher Scientific	Cat# 12-4031-82; RRID: AB_470042
Antibody	Rat anti-Ly6G	Bio X Cell	Cat# BE0075-1; RRID: AB_1107721
Recombinant protein	Annexin V PE-conjugated	Biolegend	Cat# 640908
Recombinant protein	Recombinant Murine M-CSF	PeproTech	Cat# 315-02
Chemical, compound, drug	cOmplete™, Protease Inhibitor Cocktail (PIC)	Sigma-Aldrich	Cat# 11697498001
Chemical, compound, drug	Fluoromount G® Mounting Medium	SouthernBiotech	Cat# 0100-01
Chemical, compound, drug	Matrigel® Basement Membrane Matrix	Corning	Cat# 354234
Chemical, compound, drug	Matrigel® Growth Factor Reduced (GFR) Basement Membrane Matrix, Phenol Red-free	Corning	Cat# 356231
Chemical, compound, drug	Cytochalasin D	Merck	Cat# 250255
Chemical, compound, drug	Y-27632	Merck	Cat# 688001
Chemical, compound, drug	CK-666	Merck	Cat# 182515
Chemical, compound, drug	Blebbistatin	Merck	Cat# 203390
Chemical, compound, drug	pHrodo™ Red SE	Thermo Fisher Scientific	Cat# P36600
Chemical, compound, drug	PS Lipid Microparticles	Echelon Bioscience	Cat# P-B1PS
Chemical, compound, drug	Tissue Tek™	Sakura	Cat# 4583
Chemical, compound, drug	DAPI	Sigma-Aldrich	Cat# D9542
Commercial assay, kit	Click-iT™ Plus TUNEL assay	Thermo Fisher Scientific	Cat# C10618
Commercial assay, kit	Dead Cell Removal Kit	Miltenyi Biotec	Cat# 130-090-101
Commercial assay, kit	Neutrophil Isolation Kit	Miltenyi Biotec	Cat# 130-097-658
Commercial assay, kit	Clarity™ Western ECL Substrate	Bio-Rad	Cat# 170-5060
Experimental model, mouse strain	Mouse: $Itgb1^{fl/fl}$: $Itgb1^{tm1Ref}$	(Potocnik et al., 2000), provided by R. Fässler (MPI of Biochemistry, Martinsried)	MGI:1926498
Experimental model, mouse strain	Mouse: $Tln1^{fl/fl}$: $Tln1^{tm4.1Crit}$	(Petrich et al., 2007), provided by S. Monkley and D. Critchley (University of Leicester)	MGI:3770513
Experimental model, mouse strain	Mouse: $Itgb2^{-/-}$: $Itgb2^{tm2Bay}$	(Scharffetter-Kochanek et al., 1998), provided by M. Sixt (IST, Klosterneuburg)	MGI: 1861705 JAX: 003329
Experimental model, mouse strain	Mouse: Vav-iCre: $Commd10^{Tg(Vav1\text{-}iCre)A2Kio}$	(de Boer et al., 2003), Jackson Laboratory	MGI: 2449949 JAX: 008610

Experimental model, mouse strain	Mouse: Cx3cr1^{CRE}: Cx3cr1$^{tm1.1(cre)Jung}$	(Yona et al., 2013), Jackson Laboratory	MGI: 5467983 JAX: 025524
Experimental model, mouse strain	Mouse: Lifeact-GFP: Tg(CAG-EGFP)#Rows	(Riedl et al., 2010), provided by R. Wedlich-Söldner (University of Münster)	MGI: 4831036
Experimental model, mouse strain	Mouse: Lyz2^{GFP}: Lyz2$^{tm1.1Graf}$	(Faust et al., 2000), provided by T. Graf(CRG, Barcelona)	MGI: 2654931
Experimental model, mouse strain	Mouse: Vav-iCre$^{+/-}$ Itgb1$^{fl/fl}$	In-house breeding (this paper)	
Experimental model, mouse strain	Mouse: Vav-iCre$^{+/-}$ Itgb1$^{fl/fl}$ Lyz2$^{GFP/+}$	In-house breeding (this paper)	
Experimental model, mouse strain	Mouse: Cx3cr1$^{CRE/+}$ Tln1$^{fl/fl}$	In-house breeding (this paper)	
Experimental model, mouse strain	Mouse: Cx3cr1$^{CRE/+}$ Tln1$^{fl/fl}$ Lifeact-GFP $^{+/-}$	In-house breeding (this paper)	
Software, algorithm	Adobe Illustrator 2019	Adobe	https://www.adobe.com
Software, algorithm	BD FACSDiva v6	BD	https://www.bdbioscibdbio.com/en-us/instruments/researes-instruments/research-software/flow-cytometry-acquisition/facsdiva-software
Software, algorithm	Fiji, ImageJ2	(Rueden et al., 2017; Schindelin et al., 2012)	https://imagej.net
Software, algorithm	FlowJo v10.8.0	BD	https://www.flowjo.com
Software, algorithm	GraphPad Prism Version 8	GraphPad	https://www.graphpad.com
Software, algorithm	Image Lab™ Software	Bio-Rad	https://www.bio-rad.com/de-at/product/image-lab-software
Software, algorithm	Imaris v9.5 to 9.7	Bitplane	https://imaris.oxinst.com/versions/9-5
Software, algorithm	ZEN 2012 SP5 FP3 (black)	ZEISS Microscopy	https://www.zeiss.com/microscopy/int/products/microscope-software/zen.html#modules
Software, algorithm	Incucyte Base Software	Incucyte	https://www.sartorius.com/en/products/live-cell-imaging-analysis/live-cell-analysis-software/incucyte-base-software
Software, algorithm	Incucyte Spheroid Analysis Software Module	Incucyte	https://www.sartorius.com/en/products/live-cell-imaging-analysis/live-cell-analysis-software/incucyte-base-software
Software, algorithm	Ibidi chemotaxis and migration tool	Ibidi	https://ibidi.com/chemotaxis-analysis/171-chemotaxis-and-migration-tool.html?gclid=EAIaIQobChMI2c2LtcbW8wIVgrh3Ch2B8wV9EAAYASAAEgLMbvD_BwE

Experimental Model

Mouse models

All used mouse strains and crosses were on a C57BL/6J background and are listed in the Key Resources Table. *Itgb1*$^{fl/fl}$ (Potocnik et al., 2000), *Tln1*$^{fl/fl}$ (Petrich et al., 2007), *Itgb2*$^{-/-}$ (Scharffetter-Kochanek et al., 1998), *Commd10*$^{Tg(Vav1\text{-}icre)}$ (de Boer et al., 2003), *Cx3cr1*^{CRE} (Yona et al., 2013), *Tg(Lifeact-GFP)* (Riedl et al., 2010), and *Lyz2*^{GFP} (Faust et al., 2000) mouse strains have been described elsewhere. Mice were maintained in a conventional animal facility at the Max Planck Institute of Immunobiology and Epigenetics according to local regulations. Animal breeding and husbandry were performed in accordance with the guidelines provided by the Federation of European Laboratory Animal Science Association and by German authorities and the Regional Council of Freiburg. All mouse strains in this study were without health burden. Mouse strains without fluorescent reporter lines and mouse crosses with *Tg(Lifeact-GFP)* were only used for organ removal after euthanasia by carbon dioxide exposure. *Vav-iCre Itgb1*$^{fl/fl}$ *Lyz2*$^{GFP/+}$ and WT *Lyz2*$^{GFP/+}$ control mice were used for two-photon intravital microscopy. Adult mice (>8 weeks) were age– and sex-matched in all experiments, and littermate animals were used as controls in most experiments. For Cre-expressing mouse strains, Cre-expressing littermate control animals were preferred. A contribution of Cre expression to biological phenotypes was never observed and ruled out through control experiments. Intravital imaging experiments were performed according to study protocols approved by the German authorities and the Regional Council of Freiburg (35-9185.81/G-18/111).

Method details

Ear skin and dura mater whole mount staining

Whole mounts of murine ear skin were prepared by splitting the ear in half and by separating the dermal tissue from the cartilage. Split ears were fixed in 1 % PFA in PBS for 16 h at 4 °C. The tissue was then blocked and permeabilized by incubating it in wash/staining solution (0.2 % Triton™ X-100, 1 % bovine serum albumin (BSA; Sigma Aldrich) in PBS) for 16 h on a plate shaker. Primary antibody staining was performed for 16 h shaking at 4 °C. Subsequently, the tissue was washed three times for 15 min at room temperature in wash/staining solution. Samples were stained with secondary antibody solution for 16 h shaking at 4 °C, followed by an additional three washing steps. To isolate dura mater whole mounts, the cranium skull together with the dura mater were dissected and placed in 4% PFA for 4 h at 4 °C. The Dura mater was then peeled away from the cranium skull bones and stained in the same manner as ear skin whole mounts. Antibodies used for labeling ear skin

whole mounts were: anti-collagen IV (1:500, abcam), anti-rabbit Alexa Fluor 405 (1:300, Thermo Fisher Scientific), and anti-CD206 (1:200, Biolegend). Antibodies used for labeling dura maters were: anti-Iba1 (1:200, Wako), anti-collagen IV (1:200, Merck Millipore), anti-goat Alexa Fluor 488 (1:300, Thermo Fisher Scientific) and anti-rabbit Alexa Fluor 568 (1:300, Thermo Fisher Scientific). The tissues were mounted on Superfrost™ glass slides (Thermo Fisher Scientific) with a coverglass and Fluoromount-G (SouthernBiotech). Image acquisition was performed using a LSM 780 microscope (Zeiss) with a Plan-Apochromat 20× M27 objective (Zeiss) as well as with a Plan-Apochromat 40×/1.4 Oil DIC M27 objective.

Mouse bone marrow-derived macrophage culture

Bone marrow-derived mouse macrophages (BMDM) were generated from bone marrow precursors by standard M-CSF culture. Os coxae, tibia and femora were dissected from mice and the bone marrow flushed with RPMI. The resulting bone marrow suspension was passed through a 70 µm filter and pelleted in a centrifuge at 330 x g for 5 min. Upon re-suspension cells were counted and re-suspended at 5×10^6 cells/ml in heat-inactivated fetal calf serum (FCS) with 10 % DMSO and stored at −80 °C until usage. For macrophage differentiation, frozen bone marrow cells were defrosted, washed once with 20 ml RPMI (37 °C) at 330 × g for 5 min and re-suspended in 10 ml of macrophage medium (RPMI, 10 % FCS, 1 % penicillin/streptomycin and 20 ng/ml M-CSF). The cell suspension was plated on a 10 cm petri dish and incubated at 37 °C, 5 % CO_2 (day 0). On days 3 and 5 of the culture, 5 ml of fresh macrophage medium was added on top of the pre-existing medium. Cells were harvested with 20 mM EDTA at day 6 of differentiation. Dead cells were removed using a dead cell removal kit (Miltenyi Biotec) prior to any experiment, in accordance with the manufacturer's instructions.

Flow cytometry

BMDMs were harvested as described before and Fc receptors were blocked with an anti-mouse CD16/CD32 antibody (1:250, BD Biosciences) in FACS buffer (5 % heat-inactivated FCS, 2 mM EDTA in PBS) for 10 min at room temperature. Cells were stained with the desired antibody cocktail for 30 min on ice, followed by 3 wash steps with FACS buffer (5 min at 300 × g). Cells were resuspended in DAPI solution (0.5 µg DAPI in FACS buffer) and incubated for 10 min at room temperature. The cells were then analyzed using an LSR III or LSRFortessa™ (BD Biosciences) flow cytometer. Data were processed with the FlowJo™ software (BD Bioscience), where the integrin expression of living (DAPI negative) F4/80-expressing cells (1:100, Invitrogen) was analyzed. Antibodies used were: PE-conjugated anti-CD29 (1:400, Biolegend), PE-conjugate anti-CD11b (1:400, BD Bioscience), Alexa Fluor 488-conjugated anti-CD49f (1:400, Biolegend), rat IgG2a kappa isotype control (1:400,

Thermo Scientific), armenian hamster IgG isotype control (1:400, Biolegend), rat IgG1 kappa isotype control (1:400, Thermo Fisher Scientific), anti-integrin β7 chain (1:400, BD Bioscience), rat IgG2a isotype control (1:400, Thermo Fisher Scientific), rat IgG2b kappa Isotype control (1:400, Thermo Fisher Scientific), anti-CD18 (1:400, BD Bioscience), anti-CD49d (1:400, Thermo Scientific), anti-CD51 (1:400, BD Bioscience), anti-CD61 (1:400, BD Bioscience), anti-CD49e (1:400, BD Bioscience) and rat IgG1 kappa isotype control (1:400, Thermo Fisher Scientific). To assess phagocytosis of macrophages in suspension, a 2:1 ratio of fluorescent phosphatidylserine-attached beads and BMDMs suspended in macrophage medium were incubated for 2 h on a shaker at 37 °C and 700 rpm. Afterwards cells were Fc blocked in annexin-binding buffer (135 mM NaCl, 5 mM KCl, 5.6 mM glucose, 1.8 mM $CaCl_2$, 1 mM $MgCl_2$ and 20 mM HEPES, pH 7.3) using CD16/32 blocking antibodies (1:250, BD Biosciences), which was followed by labeling in annexin-binding buffer with anti-F4/80 antibodies (1:100, Invitrogen) and annexin V (1:50, Biolegend) for 25 min at 4 °C. Cells were then washed two times and re-suspended in annexin-binding buffer containing 0.5 µg/ml DAPI. Results were acquired by flow cytometry using an LSR III (BD Biosciences) and analyzed using FlowJo™ software (BD Bioscience). Since internalization of phosphatidylserine-attached beads by BMDMs would shield them from annexin V labeling, cells which had acquired a green bead florescence signal, but were still annexin V negative, where defined as having internalized beads.

Immunoblot analysis

For immunoblot analysis, 5×10^5 BMDMs were lysed in RIPA buffer (50 mM Tris-HCl, 150 mM NaCl, 0.5 % (v:v) NP40, 1 % (v:v) Triton™ X-100, 5 mM EGTA, 5 mM EDTA, 1x cOmplete™ protease inhibitor cocktail) for 15 min on ice with regular pipetting. Proteins were separated by SDS-PAGE (BioRad) on a 12 % polyacrylamide gel, followed by a semi-dry transfer onto a PVDF membrane (Millipore). Nonspecific binding sites were blocked with Tris-buffered saline (TBS) containing 5 % BSA and 0.1 % (v:v) Tween-20. The membrane was incubated with antibodies against pan-talin (1:1000, Sigma-Aldrich) or actin (1:2000, Sigma-Aldrich) in 0.1 % Tween-20 and 5 % BSA overnight at 4 °C on a shaker. After three washes for 15 min in 0.7 % Tween-20 in PBS, the membrane was incubated in secondary antibody solutions (TBS containing 0.1 % Tween-20 and 5 % BSA, HRP-conjugated secondary antibodies (1:5000, Dako)) at room temperature. Protein bands were visualized with Clarity Western ECL substrate (BioRad), using a ChemiDoc™ Touch Gel Imaging System (Bio-Rad).

Mouse neutrophil preparation for efferocytosis assay

Neutrophils were purified from freshly isolated mouse bone marrow cell suspensions using an autoMACS pro-selector cell separator with a MACS neutrophil isolation kit for negative selection in accordance with the manufacturer's instructions (Miltenyi Biotec). Neutrophils were aged overnight in serum-free medium at 3×10^6 cells/ml at 37 °C and 5 % CO_2. Aged neutrophils were stained prior to use in the 3D efferocytosis assay with 1 ml of 10 µg/ml pHrodo™ Red SE in HBSS per 2×10^6 cells for 45 min at 37 °C. Cells were then washed twice with RPMI.

Random migration, efferocytosis and bead uptake in 3D matrigel

For 3D random migration, efferocytosis and bead uptake assays, BMDMs were seeded at a concentration of 2.4×10^5 cells/ml in 40 % Matrigel™ supplemented with 20 ng/ml M-CSF in a 96-well Incucyte™ image lock plate on ice under sterile conditions. When required, inhibitors were added to the final Matrigel™ at given concentrations (30 µM Y27632, 2 µM Cytochalasin D, 100 µM CK-666 or 60 µM Blebbistatin). For 3D efferocytosis and bead uptake assays, aged fluorescent neutrophils or 3 µm sized phosphatidylserine-attached fluorescent beads (Echelon Biosciences) were added to the final Matrigel™ cell suspension at 4×10^5 neutrophils or $2–2.4 \times 10^5$ beads per ml, respectively. After adding Matrigel™ solution to wells of the ice cold 96-well Incucyte™ image lock plates, the plates were centrifuged for 3 min at 75 × g and 4 °C to bring the macrophages into the same focal plane for imaging. This step was required because the Incucyte™ S3 live-cell analysis system operates with an autofocus mode. Plates were then transferred to a 37 °C cell incubator to initiate the fast polymerization process of the Matrigel™ matrix and kept for 30 min to ensure complete polymerization of the gel. In this experimental setup the majority of macrophages moves over 24 hours primarily in the lower part of the gel, but cells also move vertically in the 3D gel and leave the autofocus plane. Samples were then left at room temperature for 10 min before 200 µl of macrophage medium, with or without the addition of inhibitors, were added on top of the Matrigel™. Assays were acquired using an Incucyte™ S3 live-cell analysis system (Sartorius). Each well was imaged in 15 min intervals for 24–30 h with the image lock module and the 20× objective. Fluorescent signals were acquired with the inbuilt dual color module 4614, with the visualization of phosphatidylserine-attached fluorescent beads in the green imaging channel or pHrodo™ Red SE labeled neutrophils in the red imaging channel. For cell morphology visualization during random migration, Lifeact-GFP expressing BMDMs were additionally acquired by fluorescent confocal microscopy after 24 h in the gel. Here, 5×10^5 macrophages/ml in 20 ng/ml M-CSF-supplemented 40% Matrigel™ were seeded in µ angiogenesis slides™ (Ibidi). Image acquisition was performed on a LSM 780 microscope (Zeiss), fitted with a Plan-Apochromat 40×/1.4 Oil DIC M27 objective.

Macrophage chemotaxis in 3D matrigel

Ibidi µ chemotaxis slides™ were used for 3D chemotaxis assays. 10 µL of Matrigel™ macrophage suspensions (40 % phenol red free growth factor reduced Matrigel™, macrophages at 3 × 10^6 cells/ml and 20 ng/ml M-CSF) with or without inhibitors (30 µM Y27632, 2 µM Cytochalasin D or 100 µM CK-666) were added to each center port of the chemotaxis slide. The slide was then left to rest at room temperature for 7 min, followed by an incubation of 7 min at 37 °C and 5 % CO_2. The slide was finally left to settle for 5 min at room temperature. Peripheral ports on each side of the Matrigel™ were filled with 65 µL macrophage medium with or without the before mentioned inhibitors. The slides were incubated for 1 h at 37 °C and 5 % CO_2. A C5a gradient was subsequently generated by adding 15 µl macrophage medium (with or without inhibitors) containing 60 nM C5a to both ports on one side of the Matrigel™. On the opposite side, 15 µL macrophage medium were added to both ports (with or without inhibitors). The slide was then loaded into the Incucyte™ S3 live-cell analysis system (Sartorius) using a custom-made slide mount and cells were imaged using the spheroid module in 15 min intervals for 24–30 h with the 20× objective.

Tissue processing and immunofluorescence staining

Organs (spleen, liver, lymph nodes) were harvested and placed in 1 % PFA at 4 °C overnight. After incubation in a 30 % sucrose solution for 8 h, organs were embedded in molds with Tissue Tek™ and stored at −20 °C. A Leica™ CM3050 S Cryostat was used to cut tissue into 20 µm thin tissue sections, which were mounted on Superfrost™ glass slides and stored at −20 °C until further processing. For immunofluorescence stainings, samples were blocked in blocking/staining solution (0.1 % Triton™ X-100, 1 % BSA in PBS) for 2 h at room temperature. The blocking buffer was removed and the tissue was stained overnight with primary antibodies in staining solution in a humidified chamber at 4 °C. Slides were washed three times with PBS before being incubated for 4 h in a humidified chamber with the secondary antibodies in staining solution. After staining, the slides were washed a further three times in PBS and mounted with a coverglass using Fluoromount-G (SouthernBiotech). Liver and spleen sections were stained with anti-collagen IV (1:500, abcam), anti-rabbit Alexa Fluor 405 (1:200, Thermo Fisher Scientific) and PE-conjugated anti-F4/80 (1:100, Thermo Fisher Scientific) antibodies. In addition to staining with anti-collagen IV (1:500, abcam) and anti-rabbit Alexa Fluor 405 (1:200, Thermo Fisher Scientific) antibodies, the endogenous GFP expression of lymph node sections from *Lyz2*$^{GFP/+}$ containing mice were amplified using an anti-GFP Dylight™ 488 antibody (1:750, Rockland). TUNEL stainings of lymph node sections were carried out using the Click-iT™ Plus TUNEL assay kit (Invitrogen). Tissue sections were treated with 2 % H_2O_2 in methanol for 20 min at room temperature,

followed by 2 washes in PBS. Samples were permeabilized with 0.01 % Triton™ X-100, 0.1 % sodium citrate in deionized water. The tissue was then rinsed with deionized water and incubated for 10 min with terminal deoxynucleotidyl transferase (TdT) buffer at 37 °C. The TdT buffer was replaced with the TdT reaction mix and samples were incubated for 60 min at 37 °C. Tissue sections were rinsed again with deionized water and treated with 0.1 % Triton™ X-100, 3 % BSA in PBS for 5 min. Subsequently, samples were rinsed once with PBS and incubated with the TUNEL reaction cocktail for 30 min at 37 °C. Finally, the tissue sections were washed once with 3 % BSA in PBS followed by one rinse with PBS. Antibody staining was then performed on the tissue sections as mentioned above. Antibodies used were: anti-LYVE1 (1:200, Abcam), anti-CD68 (1:200, BioLegend), anti-B220 (1:200 BD Horizon), anti-GFP Dylight™ 488 (1:500, Rockland), anti-collagen IV (1:500, Abcam), anti-rabbit Alexa Fluor 405 (1:300, Thermo Fisher Scientific) and anti-F4/80 (1:100, Invitrogen). Images were acquired using an LSM 780 microscope (Zeiss) equipped with a Plan-Apochromat 20× M27 objective (Zeiss) or a Plan-Apochromat 40×/1.4 Oil DIC M27 objective.

Imaging analysis

Tracking analysis was performed with the manual tracking function of Imaris 9.5.1 to 9.7.1 (Bitplane). For the random 3D migration assays, viable cells in a randomly chosen region were manually tracked on a frame-by-frame basis. Cells that underwent cell division during the imaging period were excluded. For the 3D chemotaxis assays, BMDMs on the side of the gel facing the C5a gradient were tracked. In rare cases, biological replicates were excluded from analysis when macrophages did not respond to the attractant and only very few control cells performed directed migration. Track visualizations for random migration were generated using the Imaris spot module. Visualizations of macrophage chemotaxis tracks were generated by exporting track coordinates from Imaris and by importing them into the Ibidi chemotaxis and migration tool software. Static tissue images were visualized using the Imaris volume and surface features. Cell circularity was manually measured using ImageJ/Fiji and the freehand selection tool, drawing the outline of the cell for every frame. Macrophage scanning and area coverage was visualized by creating binary masks for each frame of the phase contrast channel using the ImageJ MorphoLibJ plugin. Binary images of all time points were combined using the Time-Lapse Color Coder plugin. The time projection image was then merged with the phase contrast and green fluorescence (beads) channel. The spot function of Imaris was used to generate spots for all green events. All spots that resided within macrophages (as defined by the phase contrast channel) were manually removed, so that only extracellular (non-cleared beads) were visualized. For the 2P-IVM analysis of the dermal macrophage chemotactic response, cell bodies of dermal macrophages were manually tracked over 90 minutes. Cell protrusions were tracked from the

onset of protrusion formation until protrusions reached their maximum extension. All protrusions from all biological replicates were tracked and the results statistically analysed. Bead uptake and neutrophil efferocytosis analysis was performed with the in-built analysis software of the Incucyte S3 instrument. Optimal parameters were manually defined for an analysis batch. Following this, a mask of the fluorescent signal was generated for all wells and time points. Within these masks, object counts and florescence intensity were analyzed. For the neutrophil efferocytosis assays, the Incucyte analysis results were further validated using an Imaris spot function analysis. Here, start and endpoint neutrophil florescence signals were used to generate spots for each neutrophil, which were then manually assigned as being either inside or outside of a macrophage. Using these designations the percentage removal of neutrophils was calculated. Cell protrusiveness was analyzed using a modified timeseries-based Sholl analysis and performed by tracking 10 random cells per condition. This entailed overlaying each cells center points with a bullseye containing concentric rings (Sholl shells) at 25 µm intervals. The number of occasions a Sholl shell was intersected by a cellular process was counted for all 15 min time intervals in a 24 h timeframe. This type of analysis was able to capture both multiple branch-based and elongation-based protrusiveness (Figure 5 – figure supplement 2). The TUNEL assay analysis was performed with ImageJ. T cell zones (B220-, and LYVE1-negative regions) were marked as regions of interest (ROI). The number of TUNEL-positive events in the ROI, which did not overlap with a $CD68^{+}$ macrophage stain, was quantified using the multi-point counter on a *z*-projection.

Two-photon intravital microscopy of macrophage chemotaxis

2P-IVM of directed macrophage migration toward a sterile laser-induced wound injury was performed in the absence of neutrophils. To avoid any contribution of neutrophils to this response, neutrophils were depleted by one intraperitoneal injection with 200 µg of anti-Ly6G antibody diluted in PBS the day before imaging. Macrophage populations were visualized by GFP fluorescence in *Vav-iCre Itgb1*$^{fl/fl}$ *Lyz2*$^{GFP/+}$ and WT *Lyz2*$^{GFP/+}$ mice. For the experiment mice were anesthetized using isoflurane (cp-pharma; the isoflurane was vaporized in an oxygen-air mixture; 2 % isoflurane was used for induction and 1–1.5 % was used for maintenance). The anesthetized mouse was placed in a lateral recumbent position on a custom-made imaging platform, so that the ventral side of the ear pinna rested on a coverslip. The ear was immobilized with a strip of Hansaplast tape, which was lightly stretched over the ear and the imaging platform. 2P-IVM was performed using a LSM 780 NLO microscope (Zeiss) enclosed in a custom-built environmental chamber that was maintained at 32°C using heated air (Kienle et al., 2021). Anesthetized mice were kept in the heated environmental chamber for 15 to 30 min until the ear tissue had settled. Once the tissue was stable, a focal skin injury was induced by a focused 2P laser pulse at an

approximate laser intensity of 80 mW. A circular region of interest of 15–30 µm in diameter was defined in one focal plane of the collagenous ear dermis, followed by laser scanning at 920 nm wavelength until tissue coagulation started within 1–3 seconds. Image acquisition was started immediately after laser-induced tissue damage. A water immersion C-Apochromat 40×/1.2 with corrector M27 objective was used for image acquisition. The microscope system was fitted with four external non-descanned photomultiplier tube detectors in the reflected light path. Fluorescence excitation was provided by an Insight® Ds+™ (Spectra Physics) tuned to 920 nm for GFP excitation and the generation of collagen second harmonic signal. Non-descanned detectors collected the emitted light. Images were mainly captured towards the anterior half of the ear pinna where hair follicles are sparse. For four-dimensional data sets, three-dimensional stacks were captured every 1 min. Raw imaging data were processed with Imaris software version 9.1.2 (Bitplane). All movies are displayed as two-dimensional maximum-intensity projections of 10–15 µm thick *z*-stacks. As the laser ablation turns the circular injured tissue autofluorescent in several channels, we masked the GFP autofluorescence of this region with Imaris-based image processing for data presentation.

Statistics

Sample size was determined prior to experiment for all experiments used for hypothesis testing (i.e. data that include statistical inference). Technical replicates of one biological replicate were designated with “N“, biological replicates were designated with “n“. Sample sizes for technical replicates (i.e. the tracking of randomly chosen migrating cells) in one biological replicate were considered based on the mean and standard deviation of WT macrophage speed during migration. We defined a 30% reduction of mean speed at a power of 0.95 as biologically meaningful effect, determining a sample size of N=25. Reproducibility of the experimental findings was verified using biological replicates, which were performed as independent experiments. Experimental groups were defined by inhibitor treatment or by the genotype. Sample sizes for biological replicates in cell culture experiments (i.e. BMDM cultures generated from different individual mice) aimed for a minimum of mouse donors to reduce the number of laboratory animals. Sample size for animal experimentation was determined according to animal welfare guidelines. Blinding was not relevant for experiments with genotyping groups because all experimental groups were treated the same. Unpaired two-tailed t tests and analysis of variance (ANOVA) were performed after data were confirmed to fulfill the criteria of normal distribution, otherwise two-tailed Mann–Whitney U tests or Kruskal–Wallis tests were applied. The D’Agostino & Pearson normality test was performed for group sizes over ten, for group sizes under ten the Shapiro-Wilk normality test was performed. If overall ANOVA or Kruskal–Wallis tests were significant, we performed post

hoc test with pair-wise comparisons (ANOVA: Dunnett, Kruskal–Wallis: Dunn). Analyses were performed with GraphPad Prism-software (Version 8.3.1). Asterisks indicate significance (*$P \leq 0.05$, **$P \leq 0.01$, ***$P \leq 0.001$). NS indicates non-significant difference ($P > 0.05$). For further statistical details, see Supplementary Table 1.

Acknowledgements

We thank K. Ganter for technical assistance and A. Rambold, J. Zimmermann and K. Glaser for critically reading the manuscript. We thank R. Fässler, C. Brakebusch, R. Wedlich-Söldner, S. Monkley, D. Critchley, M. Sixt and T. Graf for providing mouse lines for this study. This work was funded by the Deutsche Forschungsgemeinschaft (DFG, German Research Foundation), Project-IDs 259373024 (CRC/TRR 167) and 89986987 (SFB 850), and by the Max Planck Society.

Author contribution

N.P.: Conceptualization; Investigation; Methodology; Formal analysis; Validation; Visualization; Writing - review and editing. T.L.: Conceptualization, Funding acquisition, Project administration, Supervision, Investigation, Formal analysis, Methodology, Visualization, Writing - original draft, Writing – review and editing.

Declaration of Interests

The authors declare no competing financial or non-financial interests.

References

Arasa, J., Collado-Diaz, V., Kritikos, I., Medina-Sanchez, J. D., Friess, M. C., Sigmund, E. C., Schineis, P., Hunter, M. C., Tacconi, C., Paterson, N., Nagasawa, T., Kiefer, F., Makinen, T., Detmar, M., Moser, M., Lammermann, T., & Halin, C. (2021, Jul 5). Upregulation of VCAM-1 in lymphatic collectors supports dendritic cell entry and rapid migration to lymph nodes in inflammation. *J Exp Med, 218*(7). https://doi.org/10.1084/jem.20201413

Asokan, S. B., Johnson, H. E., Rahman, A., King, S. J., Rotty, J. D., Lebedeva, I. P., Haugh, J. M., & Bear, J. E. (2014, Dec 22). Mesenchymal chemotaxis requires selective inactivation of myosin II at the leading edge via a noncanonical PLCgamma/PKCalpha pathway. *Dev Cell, 31*(6), 747-760. https://doi.org/10.1016/j.devcel.2014.10.024

Baratin, M., Simon, L., Jorquera, A., Ghigo, C., Dembele, D., Nowak, J., Gentek, R., Wienert, S., Klauschen, F., Malissen, B., Dalod, M., & Bajenoff, M. (2017, Aug 15). T Cell Zone Resident Macrophages Silently Dispose of Apoptotic Cells in the Lymph Node. *Immunity, 47*(2), 349-362 e345. https://doi.org/10.1016/j.immuni.2017.07.019

Barros-Becker, F., Lam, P. Y., Fisher, R., & Huttenlocher, A. (2017, Nov 15). Live imaging reveals distinct modes of neutrophil and macrophage migration within interstitial tissues. *J Cell Sci, 130*(22), 3801-3808. https://doi.org/10.1242/jcs.206128

Bellomo, A., Gentek, R., Bajenoff, M., & Baratin, M. (2018, Aug). Lymph node macrophages: Scavengers, immune sentinels and trophic effectors. *Cell Immunol, 330*, 168-174. https://doi.org/10.1016/j.cellimm.2018.01.010

Bleriot, C., Chakarov, S., & Ginhoux, F. (2020, Jun 16). Determinants of Resident Tissue Macrophage Identity and Function. *Immunity, 52*(6), 957-970. https://doi.org/10.1016/j.immuni.2020.05.014

Bodor, D. L., Ponisch, W., Endres, R. G., & Paluch, E. K. (2020, Mar 9). Of Cell Shapes and Motion: The Physical Basis of Animal Cell Migration. *Dev Cell, 52*(5), 550-562. https://doi.org/10.1016/j.devcel.2020.02.013

Brand, A., Diener, N., Zahner, S. P., Tripp, C., Backer, R. A., Karram, K., Jiang, A., Mellman, I., Stoitzner, P., & Clausen, B. E. (2020, Jan). E-Cadherin is Dispensable to Maintain Langerhans Cells in the Epidermis. *J Invest Dermatol, 140*(1), 132-142 e133. https://doi.org/10.1016/j.jid.2019.06.132

Calderwood, D. A., & Ginsberg, M. H. (2003, Aug). Talin forges the links between integrins and actin. *Nat Cell Biol, 5*(8), 694-697. https://doi.org/10.1038/ncb0803-694

Comber, K., Huelsmann, S., Evans, I., Sanchez-Sanchez, B. J., Chalmers, A., Reuter, R., Wood, W., & Martin-Bermudo, M. D. (2013, Aug 1). A dual role for the betaPS integrin myospheroid in mediating Drosophila embryonic macrophage migration. *J Cell Sci, 126*(Pt 15), 3475-3484. https://doi.org/10.1242/jcs.129700

Cox, N., Pokrovskii, M., Vicario, R., & Geissmann, F. (2021, Apr 26). Origins, Biology, and Diseases of Tissue Macrophages. *Annu Rev Immunol, 39*, 313-344. https://doi.org/10.1146/annurev-immunol-093019-111748

Cui, K., Ardell, C. L., Podolnikova, N. P., & Yakubenko, V. P. (2018). Distinct Migratory Properties of M1, M2, and Resident Macrophages Are Regulated by alphaDbeta2

and alphaMbeta2 Integrin-Mediated Adhesion. *Front Immunol, 9*, 2650. https://doi.org/10.3389/fimmu.2018.02650

Damisah, E. C., Hill, R. A., Rai, A., Chen, F., Rothlin, C. V., Ghosh, S., & Grutzendler, J. (2020, Jun). Astrocytes and microglia play orchestrated roles and respect phagocytic territories during neuronal corpse removal in vivo. *Sci Adv, 6*(26), eaba3239. https://doi.org/10.1126/sciadv.aba3239

Davidson, A. J., & Wood, W. (2020a, May 26). Macrophages Use Distinct Actin Regulators to Switch Engulfment Strategies and Ensure Phagocytic Plasticity In Vivo. *Cell Rep, 31*(8), 107692. https://doi.org/10.1016/j.celrep.2020.107692

Davidson, A. J., & Wood, W. (2020b, Apr 1). Phagocyte Responses to Cell Death in Flies. *Cold Spring Harb Perspect Biol, 12*(4). https://doi.org/10.1101/cshperspect.a036350

Dawson, C. A., Pal, B., Vaillant, F., Gandolfo, L. C., Liu, Z., Bleriot, C., Ginhoux, F., Smyth, G. K., Lindeman, G. J., Mueller, S. N., Rios, A. C., & Visvader, J. E. (2020, May). Tissue-resident ductal macrophages survey the mammary epithelium and facilitate tissue remodelling. *Nat Cell Biol, 22*(5), 546-558. https://doi.org/10.1038/s41556-020-0505-0

de Boer, J., Williams, A., Skavdis, G., Harker, N., Coles, M., Tolaini, M., Norton, T., Williams, K., Roderick, K., Potocnik, A. J., & Kioussis, D. (2003, Feb). Transgenic mice with hematopoietic and lymphoid specific expression of Cre. *Eur J Immunol, 33*(2), 314-325. https://doi.org/10.1002/immu.200310005

Dimchev, V., Lahmann, I., Koestler, S. A., Kage, F., Dimchev, G., Steffen, A., Stradal, T. E. B., Vauti, F., Arnold, H. H., & Rottner, K. (2021). Induced Arp2/3 Complex Depletion Increases FMNL2/3 Formin Expression and Filopodia Formation. *Front Cell Dev Biol, 9*, 634708. https://doi.org/10.3389/fcell.2021.634708

Elliott, M. R., & Ravichandran, K. S. (2016, Jul 25). The Dynamics of Apoptotic Cell Clearance. *Dev Cell, 38*(2), 147-160. https://doi.org/10.1016/j.devcel.2016.06.029

Faust, N., Varas, F., Kelly, L. M., Heck, S., & Graf, T. (2000, Jul 15). Insertion of enhanced green fluorescent protein into the lysozyme gene creates mice with green fluorescent granulocytes and macrophages. *Blood, 96*(2), 719-726. https://www.ncbi.nlm.nih.gov/pubmed/10887140

Freitas-Lopes, M. A., Mafra, K., David, B. A., Carvalho-Gontijo, R., & Menezes, G. B. (2017, Dec 7). Differential Location and Distribution of Hepatic Immune Cells. *Cells, 6*(4). https://doi.org/10.3390/cells6040048

Gawden-Bone, C., West, M. A., Morrison, V. L., Edgar, A. J., McMillan, S. J., Dill, B. D., Trost, M., Prescott, A., Fagerholm, S. C., & Watts, C. (2014, Oct 01). A crucial role for beta2 integrins in podosome formation, dynamics and Toll-like-receptor-signaled disassembly in dendritic cells. *J Cell Sci, 127*(Pt 19), 4213-4224. https://doi.org/10.1242/jcs.151167

Georgantzoglou, A., Poplimont, H., Lämmermann, T., & Sarris, M. (2021). Interstitial leukocyte navigation through a search and run response to gradients. *bioRxiv*, 2021.2003.2003.433706. https://doi.org/10.1101/2021.03.03.433706

Gordon, S., Pluddemann, A., & Mukhopadhyay, S. (2014, Dec 11). Sinusoidal immunity: macrophages at the lymphohematopoietic interface. *Cold Spring Harb Perspect Biol, 7*(4), a016378. https://doi.org/10.1101/cshperspect.a016378

Han, C. Z., Juncadella, I. J., Kinchen, J. M., Buckley, M. W., Klibanov, A. L., Dryden, K., Onengut-Gumuscu, S., Erdbrugger, U., Turner, S. D., Shim, Y. M., Tung, K. S., & Ravichandran, K. S. (2016, Nov 24). Macrophages redirect phagocytosis by non-professional phagocytes and influence inflammation. *Nature, 539*(7630), 570-574. https://doi.org/10.1038/nature20141

Honda, M., Surewaard, B. G. J., Watanabe, M., Hedrick, C. C., Lee, W. Y., Brown, K., McCoy, K. D., & Kubes, P. (2020, Mar 12). Perivascular localization of macrophages in the intestinal mucosa is regulated by Nr4a1 and the microbiome. *Nat Commun, 11*(1), 1329. https://doi.org/10.1038/s41467-020-15068-4

Hughes, L. D., Wang, Y., Meli, A. P., Rothlin, C. V., & Ghosh, S. (2021, Apr 26). Decoding Cell Death: From a Veritable Library of Babel to Vade Mecum? *Annu Rev Immunol, 39*, 791-817. https://doi.org/10.1146/annurev-immunol-102819-072601

Hynes, R. O. (2002, Sep 20). Integrins: bidirectional, allosteric signaling machines. *Cell, 110*(6), 673-687. https://doi.org/10.1016/s0092-8674(02)00971-6

Jain, R., & Weninger, W. (2013, Apr). Shedding light on cutaneous innate immune responses: the intravital microscopy approach. *Immunol Cell Biol, 91*(4), 263-270. https://doi.org/10.1038/icb.2012.76

Jaumouille, V., Cartagena-Rivera, A. X., & Waterman, C. M. (2019, Nov). Coupling of beta2 integrins to actin by a mechanosensitive molecular clutch drives complement receptor-mediated phagocytosis. *Nat Cell Biol, 21*(11), 1357-1369. https://doi.org/10.1038/s41556-019-0414-2

Jaumouille, V., & Waterman, C. M. (2020). Physical Constraints and Forces Involved in Phagocytosis. *Front Immunol, 11*, 1097. https://doi.org/10.3389/fimmu.2020.01097

Kelly, A., Gunaltay, S., McEntee, C. P., Shuttleworth, E. E., Smedley, C., Houston, S. A., Fenton, T. M., Levison, S., Mann, E. R., & Travis, M. A. (2018, Nov 5). Human monocytes and macrophages regulate immune tolerance via integrin alphavbeta8-mediated TGFbeta activation. *J Exp Med, 215*(11), 2725-2736. https://doi.org/10.1084/jem.20171491

Kienle, K., Glaser, K. M., Eickhoff, S., Mihlan, M., Knopper, K., Reategui, E., Epple, M. W., Gunzer, M., Baumeister, R., Tarrant, T. K., Germain, R. N., Irimia, D., Kastenmuller, W., & Lammermann, T. (2021, Jun 18). Neutrophils self-limit swarming to contain bacterial growth in vivo. *Science, 372*(6548). https://doi.org/10.1126/science.abe7729

Lämmermann, T., Afonso, P. V., Angermann, B. R., Wang, J. M., Kastenmuller, W., Parent, C. A., & Germain, R. N. (2013, Jun 20). Neutrophil swarms require LTB4 and integrins at sites of cell death in vivo. *Nature, 498*(7454), 371-375. https://doi.org/10.1038/nature12175

Lämmermann, T., Bader, B. L., Monkley, S. J., Worbs, T., Wedlich-Soldner, R., Hirsch, K., Keller, M., Forster, R., Critchley, D. R., Fassler, R., & Sixt, M. (2008, May 1). Rapid leukocyte migration by integrin-independent flowing and squeezing. *Nature, 453*(7191), 51-55. https://doi.org/10.1038/nature06887

Lämmermann, T., & Germain, R. N. (2014, Mar). The multiple faces of leukocyte interstitial migration. *Semin Immunopathol, 36*(2), 227-251. https://doi.org/10.1007/s00281-014-0418-8

Lämmermann, T., & Sixt, M. (2009, Oct). Mechanical modes of 'amoeboid' cell migration. *Curr Opin Cell Biol, 21*(5), 636-644. https://doi.org/10.1016/j.ceb.2009.05.003

Leithner, A., Eichner, A., Muller, J., Reversat, A., Brown, M., Schwarz, J., Merrin, J., de Gorter, D. J., Schur, F., Bayerl, J., de Vries, I., Wieser, S., Hauschild, R., Lai, F. P., Moser, M., Kerjaschki, D., Rottner, K., Small, J. V., Stradal, T. E., & Sixt, M. (2016, Nov). Diversified actin protrusions promote environmental exploration but are dispensable for locomotion of leukocytes. *Nat Cell Biol, 18*(11), 1253-1259. https://doi.org/10.1038/ncb3426

Lemke, G. (2019, Sep). How macrophages deal with death. *Nat Rev Immunol, 19*(9), 539-549. https://doi.org/10.1038/s41577-019-0167-y

Ley, K., Pramod, A. B., Croft, M., Ravichandran, K. S., & Ting, J. P. (2016). How Mouse Macrophages Sense What Is Going On. *Front Immunol, 7*, 204. https://doi.org/10.3389/fimmu.2016.00204

Matsubayashi, Y., Louani, A., Dragu, A., Sanchez-Sanchez, B. J., Serna-Morales, E., Yolland, L., Gyoergy, A., Vizcay, G., Fleck, R. A., Heddleston, J. M., Chew, T. L., Siekhaus, D. E., & Stramer, B. M. (2017, Nov 20). A Moving Source of Matrix Components Is Essential for De Novo Basement Membrane Formation. *Curr Biol, 27*(22), 3526-3534 e3524. https://doi.org/10.1016/j.cub.2017.10.001

Meller, J., Chen, Z., Dudiki, T., Cull, R. M., Murtazina, R., Bal, S. K., Pluskota, E., Stefl, S., Plow, E. F., Trapp, B. D., & Byzova, T. V. (2017, Jun 2). Integrin-Kindlin3 requirements for microglial motility in vivo are distinct from those for macrophages. *JCI Insight, 2*(11). https://doi.org/10.1172/jci.insight.93002

Moreau, H. D., Lemaitre, F., Garrod, K. R., Garcia, Z., Lennon-Dumenil, A. M., & Bousso, P. (2015, Sep 29). Signal strength regulates antigen-mediated T-cell deceleration by distinct mechanisms to promote local exploration or arrest. *Proc Natl Acad Sci U S A, 112*(39), 12151-12156. https://doi.org/10.1073/pnas.1506654112

Moreira, C. G., Jacinto, A., & Prag, S. (2013, Aug 15). Drosophila integrin adhesion complexes are essential for hemocyte migration in vivo. *Biol Open, 2*(8), 795-801. https://doi.org/10.1242/bio.20134564

Mylvaganam, S., Freeman, S. A., & Grinstein, S. (2021, May 24). The cytoskeleton in phagocytosis and macropinocytosis. *Curr Biol, 31*(10), R619-R632. https://doi.org/10.1016/j.cub.2021.01.036

Neupane, A. S., Willson, M., Chojnacki, A. K., Vargas, E. S. C. F., Morehouse, C., Carestia, A., Keller, A. E., Peiseler, M., DiGiandomenico, A., Kelly, M. M., Amrein, M., Jenne, C., Thanabalasuriar, A., & Kubes, P. (2020, Oct 1). Patrolling Alveolar Macrophages Conceal Bacteria from the Immune System to Maintain Homeostasis. *Cell, 183*(1), 110-125 e111. https://doi.org/10.1016/j.cell.2020.08.020

Nicolas-Avila, J. A., Lechuga-Vieco, A. V., Esteban-Martinez, L., Sanchez-Diaz, M., Diaz-Garcia, E., Santiago, D. J., Rubio-Ponce, A., Li, J. L., Balachander, A., Quintana, J. A., Martinez-de-Mena, R., Castejon-Vega, B., Pun-Garcia, A., Traves, P. G., Bonzon-Kulichenko, E., Garcia-Marques, F., Cusso, L., N, A. G., Gonzalez-Guerra, A., Roche-Molina, M., Martin-Salamanca, S., Crainiciuc, G., Guzman, G., Larrazabal, J.,

Herrero-Galan, E., Alegre-Cebollada, J., Lemke, G., Rothlin, C. V., Jimenez-Borreguero, L. J., Reyes, G., Castrillo, A., Desco, M., Munoz-Canoves, P., Ibanez, B., Torres, M., Ng, L. G., Priori, S. G., Bueno, H., Vazquez, J., Cordero, M. D., Bernal, J. A., Enriquez, J. A., & Hidalgo, A. (2020, Oct 1). A Network of Macrophages Supports Mitochondrial Homeostasis in the Heart. *Cell, 183*(1), 94-109 e123. https://doi.org/10.1016/j.cell.2020.08.031

Nourshargh, S., Hordijk, P. L., & Sixt, M. (2010, May). Breaching multiple barriers: leukocyte motility through venular walls and the interstitium. *Nat Rev Mol Cell Biol, 11*(5), 366-378. https://doi.org/10.1038/nrm2889

Okabe, Y., & Medzhitov, R. (2016, Jan). Tissue biology perspective on macrophages. *Nat Immunol, 17*(1), 9-17. https://doi.org/10.1038/ni.3320

Owen, K. A., Pixley, F. J., Thomas, K. S., Vicente-Manzanares, M., Ray, B. J., Horwitz, A. F., Parsons, J. T., Beggs, H. E., Stanley, E. R., & Bouton, A. H. (2007, Dec 17). Regulation of lamellipodial persistence, adhesion turnover, and motility in macrophages by focal adhesion kinase. *J Cell Biol, 179*(6), 1275-1287. https://doi.org/10.1083/jcb.200708093

Paluch, E. K., Aspalter, I. M., & Sixt, M. (2016, Oct 6). Focal Adhesion-Independent Cell Migration. *Annu Rev Cell Dev Biol, 32*, 469-490. https://doi.org/10.1146/annurev-cellbio-111315-125341

Papalazarou, V., & Machesky, L. M. (2021, Feb). The cell pushes back: The Arp2/3 complex is a key orchestrator of cellular responses to environmental forces. *Curr Opin Cell Biol, 68*, 37-44. https://doi.org/10.1016/j.ceb.2020.08.012

Petrich, B. G., Marchese, P., Ruggeri, Z. M., Spiess, S., Weichert, R. A., Ye, F., Tiedt, R., Skoda, R. C., Monkley, S. J., Critchley, D. R., & Ginsberg, M. H. (2007, Dec 24). Talin is required for integrin-mediated platelet function in hemostasis and thrombosis. *J Exp Med, 204*(13), 3103-3111. https://doi.org/10.1084/jem.20071800

Potocnik, A. J., Brakebusch, C., & Fassler, R. (2000, Jun). Fetal and adult hematopoietic stem cells require beta1 integrin function for colonizing fetal liver, spleen, and bone marrow. *Immunity, 12*(6), 653-663. https://doi.org/10.1016/s1074-7613(00)80216-2

Reversat, A., Gaertner, F., Merrin, J., Stopp, J., Tasciyan, S., Aguilera, J., de Vries, I., Hauschild, R., Hons, M., Piel, M., Callan-Jones, A., Voituriez, R., & Sixt, M. (2020, Jun). Cellular locomotion using environmental topography. *Nature, 582*(7813), 582-585. https://doi.org/10.1038/s41586-020-2283-z

Riedl, J., Flynn, K. C., Raducanu, A., Gartner, F., Beck, G., Bosl, M., Bradke, F., Massberg, S., Aszodi, A., Sixt, M., & Wedlich-Soldner, R. (2010, Mar). Lifeact mice for studying F-actin dynamics. *Nat Methods, 7*(3), 168-169. https://doi.org/10.1038/nmeth0310-168

Rothlin, C. V., & Ghosh, S. (2020, May 1). Cracking the Cell Death Code. *Cold Spring Harb Perspect Biol, 12*(5). https://doi.org/10.1101/cshperspect.a036343

Rothlin, C. V., Hille, T. D., & Ghosh, S. (2021, May). Determining the effector response to cell death. *Nat Rev Immunol, 21*(5), 292-304. https://doi.org/10.1038/s41577-020-00456-0

Rotty, J. D., Brighton, H. E., Craig, S. L., Asokan, S. B., Cheng, N., Ting, J. P., & Bear, J. E. (2017, Sep 11). Arp2/3 Complex Is Required for Macrophage Integrin Functions but

Is Dispensable for FcR Phagocytosis and In Vivo Motility. *Dev Cell, 42*(5), 498-513 e496. https://doi.org/10.1016/j.devcel.2017.08.003

Rotty, J. D., Wu, C., & Bear, J. E. (2013, Jan). New insights into the regulation and cellular functions of the ARP2/3 complex. *Nat Rev Mol Cell Biol, 14*(1), 7-12. https://doi.org/10.1038/nrm3492

Rueden, C. T., Schindelin, J., Hiner, M. C., DeZonia, B. E., Walter, A. E., Arena, E. T., & Eliceiri, K. W. (2017, Nov 29). ImageJ2: ImageJ for the next generation of scientific image data. *BMC Bioinformatics, 18*(1), 529. https://doi.org/10.1186/s12859-017-1934-z

Sanchez-Sanchez, B. J., Urbano, J. M., Comber, K., Dragu, A., Wood, W., Stramer, B., & Martin-Bermudo, M. D. (2017, Nov 7). Drosophila Embryonic Hemocytes Produce Laminins to Strengthen Migratory Response. *Cell Rep, 21*(6), 1461-1470. https://doi.org/10.1016/j.celrep.2017.10.047

Scharffetter-Kochanek, K., Lu, H., Norman, K., van Nood, N., Munoz, F., Grabbe, S., McArthur, M., Lorenzo, I., Kaplan, S., Ley, K., Smith, C. W., Montgomery, C. A., Rich, S., & Beaudet, A. L. (1998, Jul 6). Spontaneous skin ulceration and defective T cell function in CD18 null mice. *J Exp Med, 188*(1), 119-131. https://doi.org/10.1084/jem.188.1.119

Schindelin, J., Arganda-Carreras, I., Frise, E., Kaynig, V., Longair, M., Pietzsch, T., Preibisch, S., Rueden, C., Saalfeld, S., Schmid, B., Tinevez, J. Y., White, D. J., Hartenstein, V., Eliceiri, K., Tomancak, P., & Cardona, A. (2012, Jun 28). Fiji: an open-source platform for biological-image analysis. *Nat Methods, 9*(7), 676-682. https://doi.org/10.1038/nmeth.2019

Segawa, K., & Nagata, S. (2015, Nov). An Apoptotic 'Eat Me' Signal: Phosphatidylserine Exposure. *Trends Cell Biol, 25*(11), 639-650. https://doi.org/10.1016/j.tcb.2015.08.003

Stolp, B., Thelen, F., Ficht, X., Altenburger, L. M., Ruef, N., Inavalli, V., Germann, P., Page, N., Moalli, F., Raimondi, A., Keyser, K. A., Seyed Jafari, S. M., Barone, F., Dettmer, M. S., Merkler, D., Iannacone, M., Sharpe, J., Schlapbach, C., Fackler, O. T., Nagerl, U. V., & Stein, J. V. (2020, Apr 3). Salivary gland macrophages and tissue-resident CD8(+) T cells cooperate for homeostatic organ surveillance. *Sci Immunol, 5*(46). https://doi.org/10.1126/sciimmunol.aaz4371

Suraneni, P., Rubinstein, B., Unruh, J. R., Durnin, M., Hanein, D., & Li, R. (2012, Apr 16). The Arp2/3 complex is required for lamellipodia extension and directional fibroblast cell migration. *J Cell Biol, 197*(2), 239-251. https://doi.org/10.1083/jcb.201112113

Swaney, K. F., & Li, R. (2016, Oct). Function and regulation of the Arp2/3 complex during cell migration in diverse environments. *Curr Opin Cell Biol, 42*, 63-72. https://doi.org/10.1016/j.ceb.2016.04.005

Torres-Gomez, A., Cabanas, C., & Lafuente, E. M. (2020). Phagocytic Integrins: Activation and Signaling. *Front Immunol, 11*, 738. https://doi.org/10.3389/fimmu.2020.00738

Uderhardt, S., Martins, A. J., Tsang, J. S., Lämmermann, T., & Germain, R. N. (2019, Apr 18). Resident Macrophages Cloak Tissue Microlesions to Prevent Neutrophil-Driven Inflammatory Damage. *Cell, 177*(3), 541-555 e517. https://doi.org/10.1016/j.cell.2019.02.028

Van Goethem, E., Guiet, R., Balor, S., Charriere, G. M., Poincloux, R., Labrousse, A., Maridonneau-Parini, I., & Le Cabec, V. (2011, Feb-Mar). Macrophage podosomes go 3D. *Eur J Cell Biol, 90*(2-3), 224-236. https://doi.org/10.1016/j.ejcb.2010.07.011

Van Goethem, E., Poincloux, R., Gauffre, F., Maridonneau-Parini, I., & Le Cabec, V. (2010, Jan 15). Matrix architecture dictates three-dimensional migration modes of human macrophages: differential involvement of proteases and podosome-like structures. *J Immunol, 184*(2), 1049-1061. https://doi.org/10.4049/jimmunol.0902223

Vargas, P., Maiuri, P., Bretou, M., Saez, P. J., Pierobon, P., Maurin, M., Chabaud, M., Lankar, D., Obino, D., Terriac, E., Raab, M., Thiam, H. R., Brocker, T., Kitchen-Goosen, S. M., Alberts, A. S., Sunareni, P., Xia, S., Li, R., Voituriez, R., Piel, M., & Lennon-Dumenil, A. M. (2016, Jan). Innate control of actin nucleation determines two distinct migration behaviours in dendritic cells. *Nat Cell Biol, 18*(1), 43-53. https://doi.org/10.1038/ncb3284

Vorselen, D., Labitigan, R. L. D., & Theriot, J. A. (2020, Oct). A mechanical perspective on phagocytic cup formation. *Curr Opin Cell Biol, 66*, 112-122. https://doi.org/10.1016/j.ceb.2020.05.011

Weischenfeldt, J., & Porse, B. (2008, Dec 1). Bone Marrow-Derived Macrophages (BMM): Isolation and Applications. *CSH Protoc, 2008*, pdb prot5080. https://doi.org/10.1101/pdb.prot5080

Wiesner, C., Le-Cabec, V., El Azzouzi, K., Maridonneau-Parini, I., & Linder, S. (2014). Podosomes in space: macrophage migration and matrix degradation in 2D and 3D settings. *Cell Adh Migr, 8*(3), 179-191. https://www.ncbi.nlm.nih.gov/pubmed/24713854

Wood, W., & Martin, P. (2017, Feb 6). Macrophage Functions in Tissue Patterning and Disease: New Insights from the Fly. *Dev Cell, 40*(3), 221-233. https://doi.org/10.1016/j.devcel.2017.01.001

Woolf, E., Grigorova, I., Sagiv, A., Grabovsky, V., Feigelson, S. W., Shulman, Z., Hartmann, T., Sixt, M., Cyster, J. G., & Alon, R. (2007, Oct). Lymph node chemokines promote sustained T lymphocyte motility without triggering stable integrin adhesiveness in the absence of shear forces. *Nat Immunol, 8*(10), 1076-1085. https://doi.org/10.1038/ni1499

Wu, C., Asokan, S. B., Berginski, M. E., Haynes, E. M., Sharpless, N. E., Griffith, J. D., Gomez, S. M., & Bear, J. E. (2012, Mar 2). Arp2/3 is critical for lamellipodia and response to extracellular matrix cues but is dispensable for chemotaxis. *Cell, 148*(5), 973-987. https://doi.org/10.1016/j.cell.2011.12.034

Yakubenko, V. P., Lishko, V. K., Lam, S. C., & Ugarova, T. P. (2002, Dec 13). A molecular basis for integrin alphaMbeta 2 ligand binding promiscuity. *J Biol Chem, 277*(50), 48635-48642. https://doi.org/10.1074/jbc.M208877200

Yamada, K. M., & Sixt, M. (2019, Dec). Mechanisms of 3D cell migration. *Nat Rev Mol Cell Biol, 20*(12), 738-752. https://doi.org/10.1038/s41580-019-0172-9

Yona, S., Kim, K. W., Wolf, Y., Mildner, A., Varol, D., Breker, M., Strauss-Ayali, D., Viukov, S., Guilliams, M., Misharin, A., Hume, D. A., Perlman, H., Malissen, B., Zelzer, E., & Jung, S. (2013, Jan 24). Fate mapping reveals origins and dynamics of monocytes and tissue macrophages under homeostasis. *Immunity, 38*(1), 79-91. https://doi.org/10.1016/j.immuni.2012.12.001

Zajd, C. M., Ziemba, A. M., Miralles, G. M., Nguyen, T., Feustel, P. J., Dunn, S. M., Gilbert, R. J., & Lennartz, M. R. (2020). Bone Marrow-Derived and Elicited Peritoneal Macrophages Are Not Created Equal: The Questions Asked Dictate the Cell Type Used. *Front Immunol, 11*, 269. https://doi.org/10.3389/fimmu.2020.00269

Figure 1

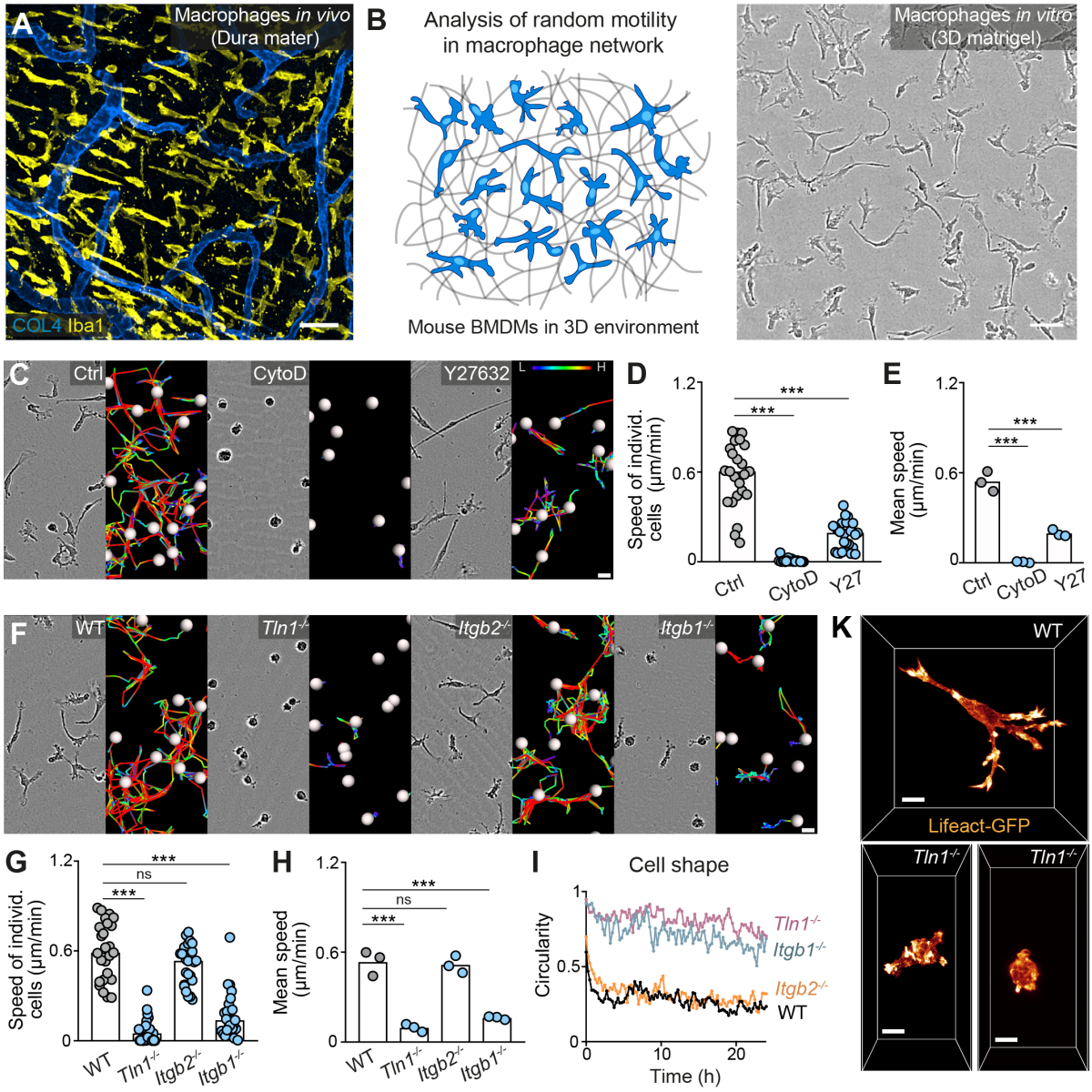

Figure 1. Haptokinetic random motility of macrophages in 3D matrices. (A) Representative macrophage network in adult mouse tissue. Immunofluorescence staining of a Dura mater whole mount preparation, showing macrophages (yellow) and blood vasculature (blue). COL4: collagen IV. **(B)** Scheme (left) and brightfield image (right) for studying macrophage network dynamics in 3D *in vitro* matrices. **(C–E)** Analysis of BMDM random motility in the presence of cytochalasin D (CytoD) or Y27632. (C) Representative cell morphologies (brightfield microscopy) and pseudo-colored tracks (displacement delta length: L(low)=0, H(high)=15) over 24 h. (D) Individual cell speeds from one independent experiment (dots represent randomly chosen cells per condition, *N*=25), and (E) mean speed values calculated from three biological replicates (*n*=3). **(F–H)** Analysis of BMDM random motility upon genetic interference with integrin functionality, including (F) cell morphologies and tracks over 24 h, (G) individual cell speeds from one independent experiment (*N*=25), and (H) mean speed values calculated from three biological replicates (*n*=3). **(I)** Graphical analysis of cell shape at 15-min time intervals over 24 h for integrin-mutant BMDMs. Dots are mean values of *N*=5 randomly chosen cells per genotype. A circularity value of 1 equals a perfectly circular cell. **(K)** Confocal live cell microscopy of Lifeact-GFP expressing WT or *Tln1*$^{-/-}$ BMDMs in 3D matrigel. Bars in graphs: median (D, G), mean (E, H). Statistical tests: ***$P \leq 0.001$, Dunn's multiple comparison (posthoc Kruskal-Wallis test) (D, G); ***$P \leq 0.001$, Dunnett's multiple comparison (posthoc ANOVA) (E, H). Scale bars: 50 µm (A, B), 10 µm (K), 20 µm (C, F).

Figure 1 – figure supplement 1

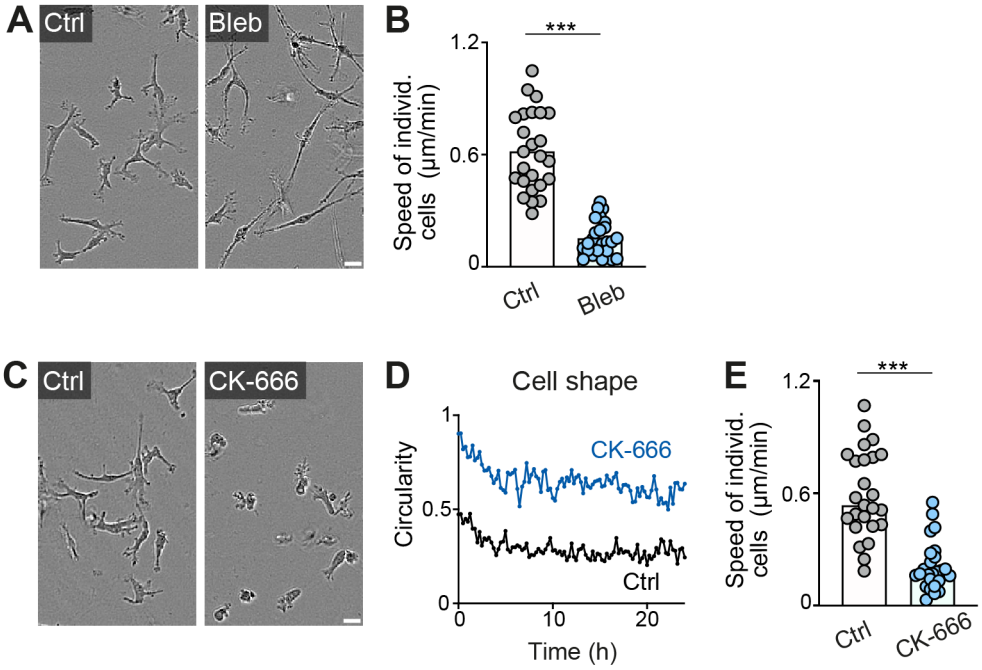

Figure 1 – figure supplement 1. Actomyosin contraction and dendritic actin networks regulate random motility of macrophages in 3D matrices. (A, B) Analysis of BMDM random motility in the presence of blebbistatin in 3D matrigel. (A) Representative cell morphologies (brightfield microscopy), (B) individual cell speeds from one independent experiment (dots represent randomly chosen cells per condition, *N*=25). Bars display the mean; ***$P \leq 0.001$, *t* test. **(C–E)** Analysis of BMDM random motility in the presence of CK-666 in 3D matrigel. (C) Representative cell morphologies (brightfield microscopy), (D) graphical analysis of cell shape at 15-min time intervals over 24 h. Dots are mean values of *N*=5 randomly chosen cells per genotype. A circularity value of 1 equals a perfectly circular cell, (E) individual cell speeds from one independent experiment (dots represent randomly chosen cells per condition, *N*=25). Bars display the median; ***$P \leq 0.001$, *U* test. Scale bars: 20 µm

Figure 1 – figure supplement 2

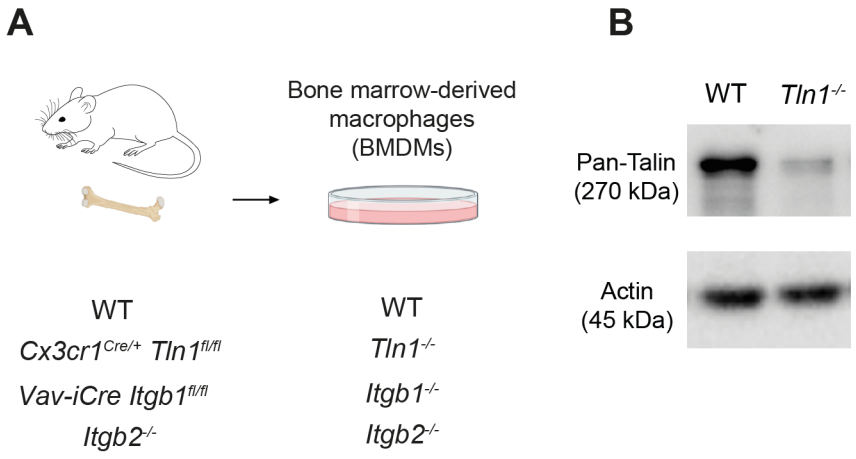

Figure 1 – figure supplement 2. Characterization of mouse bone marrow-derived macrophages with impaired integrin functionality. (A) Scheme for the generation of bone marrow-derived macrophages (BMDMs) from conditional and constitutive knockout mouse models to obtain BMDMs depleted for talin-1 (*Tln1*$^{-/-}$) or cell surface integrins from the β1 family (*Itgb1*$^{-/-}$) or β2 family (*Itgb2*$^{-/-}$). **(B)** The efficiency of conditional talin-1 knockout was confirmed by immunoblot analysis (by using a pan-talin antibody recognizing talin-1 and talin-2). Cell lysates were generated from WT and *Tln1*$^{-/-}$ BMDMs. Actin was used as loading control.

Figure 1 – figure supplement 3

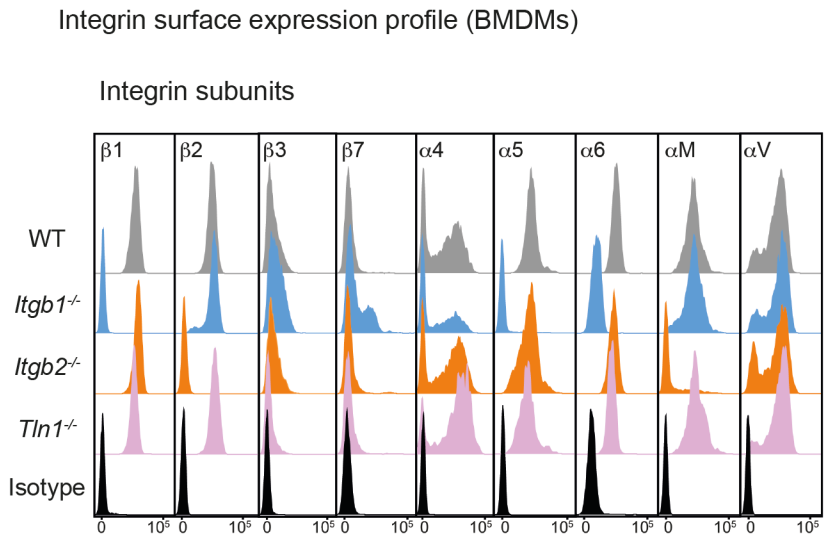

Figure 1 – figure supplement 3. Characterization of mouse bone marrow-derived macrophages with impaired integrin functionality. Flow cytometry analysis of integrin subunits expressed on the surface of WT, *Itgb1*$^{-/-}$, *Itgb2*$^{-/-}$ and *Tln1*$^{-/-}$ BMDMs. β1 integrin depletion leads to loss of fibronectin-binding α5β1 and laminin-binding α6β1 integrins from the cell surface of *Itgb1*$^{-/-}$ macrophages. A pool of the α4 subunit remains retained on the cell surface in combination with an upregulation of the corresponding β7 subunit. This switch from α4β1 to α4β7 heterodimers is a well-documented phenomenon for *Itgb1*$^{-/-}$ leukocytes. β2 integrin deficiency leads to loss of the αM subunit (CD11b) and thus αMβ2 (Mac-1, CR3) from the macrophage surface. Talin depletion in BMDMs leaves the cell surface integrin expression profile unchanged.

Figure 2

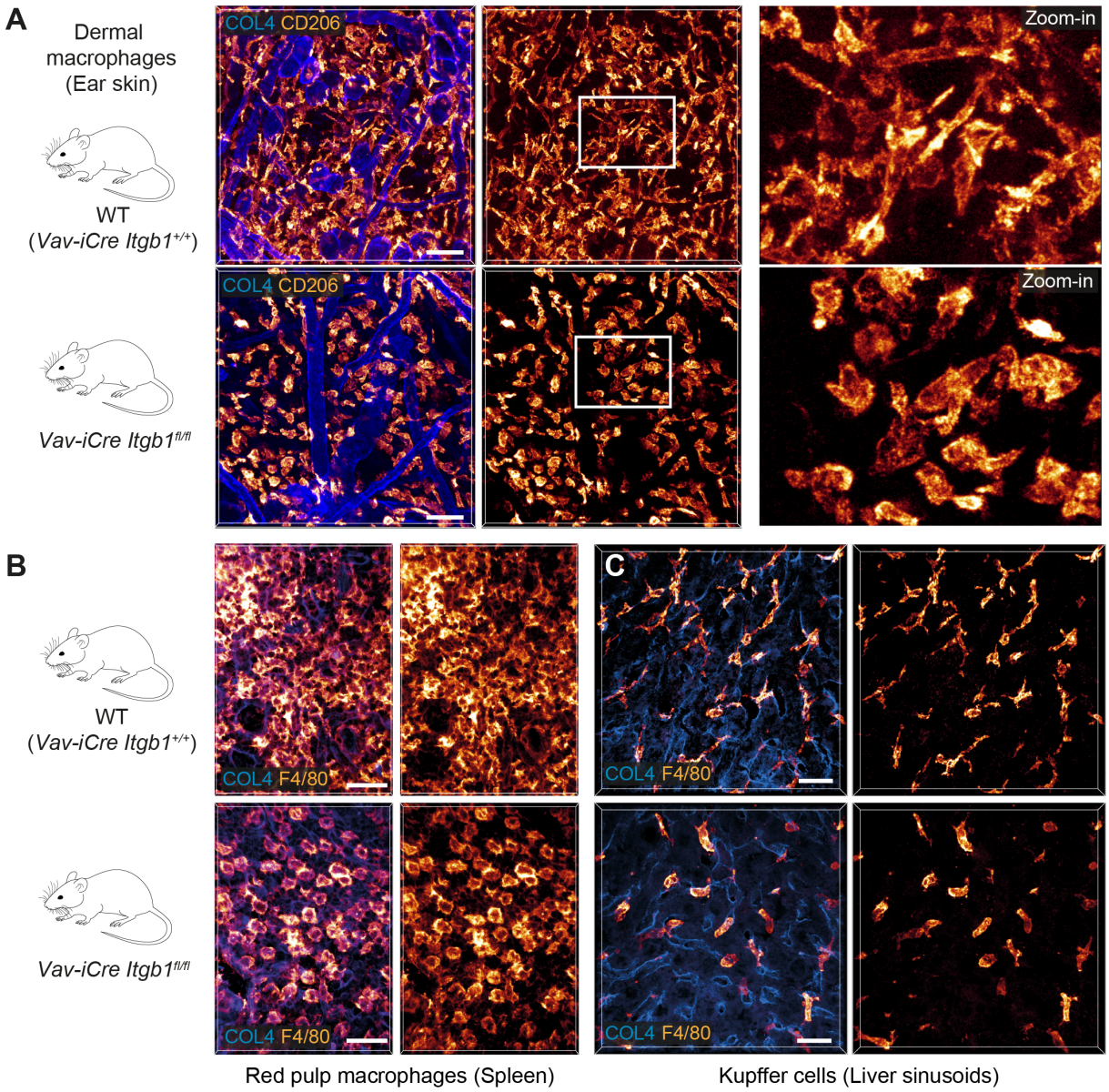

Figure 2. β1 integrins define the mesenchymal shape of macrophages in mouse tissues. (A–C) Comparative analysis of ear skin dermis (A), spleen (B) and liver (C) tissues of adult *Vav-iCre*$^{+/-}$ *Itgb1*$^{fl/fl}$ mice and littermate controls. Endogenous macrophage subsets were detected with immuno-stainings against CD206 (A) and F4/80 (B, C) and fluorescence signal intensities displayed as glow heatmap color. Collagen IV (COL4)-expressing basement membrane (A, C) or reticular network (B) structures are also displayed (blue). All images are projections of several confocal *z*-planes. Scale bars: 50 µm (A), 30 µm (B, C).

Figure 2 - figure supplement 1

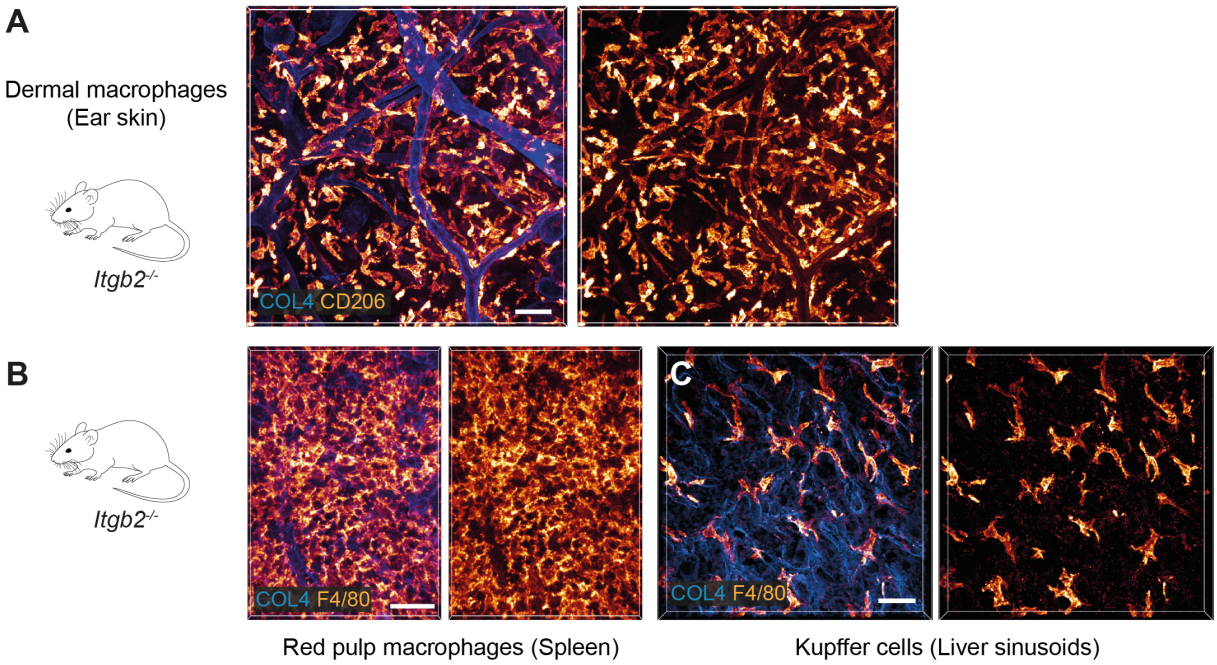

Figure 2 – figure supplement 1. β2 integrins do not contribute to the mesenchymal shape of macrophages in mouse tissues. (A–C) Immunofluorescence analysis of ear skin dermis (A), spleen (B) and liver (C) tissues of adult *Itgb2*$^{-/-}$ mice. Endogenous macrophage subsets were detected with immuno-stainings against CD206 (A) and F4/80 (B,C) and fluorescence signal intensities displayed as glow heatmap color. Collagen IV (COL4)-expressing basement membrane (A, C) or reticular network (B) structures are also displayed (blue). All images are projections of several confocal *z*-planes. Scale bars: 50 µm (A), 30 µm (B, C).

Figure 3

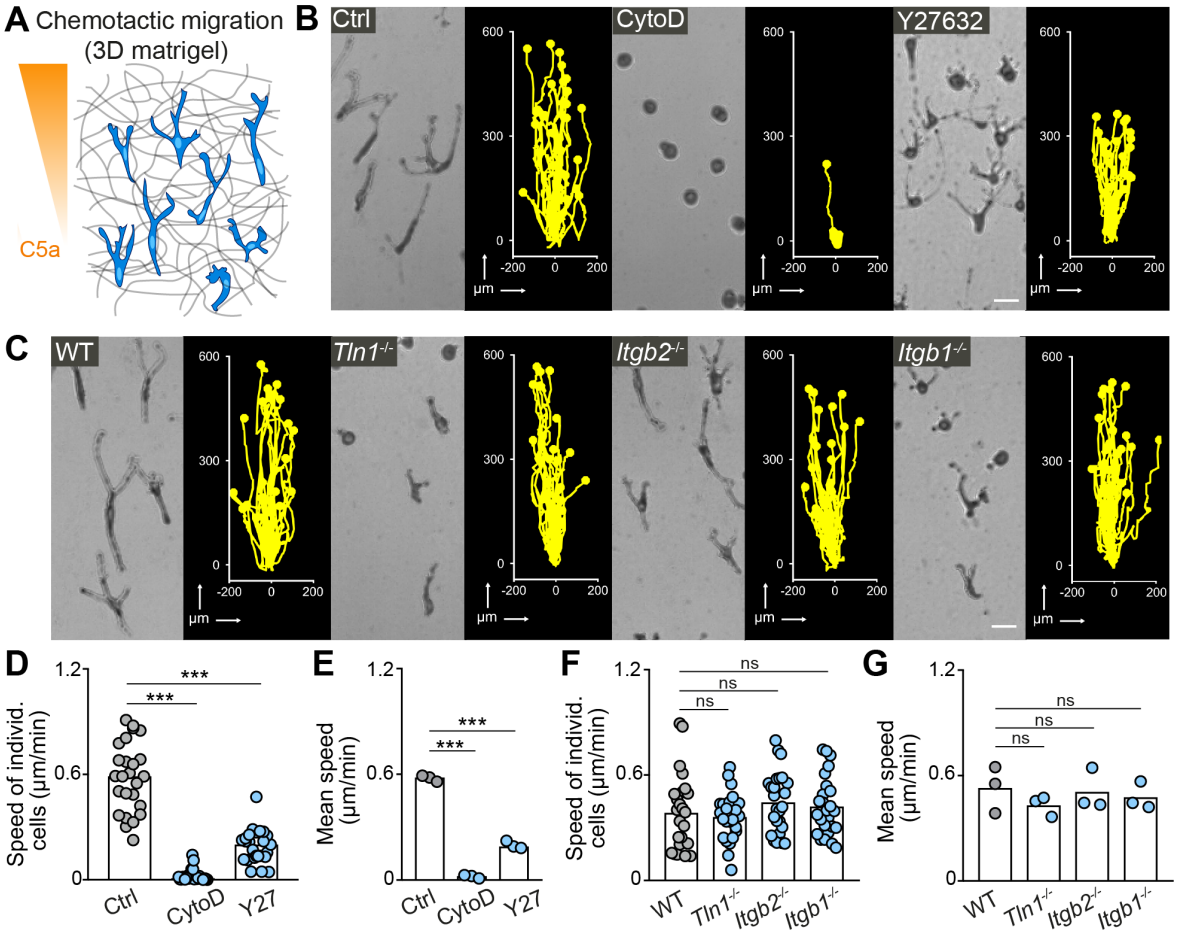

Figure 3. Integrin-independent 3D macrophage movement during chemotactic responses. (A) Scheme for studying chemotactic macrophage migration toward C5a gradients in 3D *in vitro* matrices. **(B, C)** Representative cell morphologies (brightfield microscopy) and tracks over 24 h of chemotaxing BMDMs (B) in the presence of cytochalasin D (CytoD) and Y27632, and (C) upon genetic interference with integrin functionality**.** Scale bars: 25 µm. **(D–G)** Analysis of BMDM chemotactic migration, including (D,F) individual cell speeds from one independent experiment (dots represent randomly chosen cells per condition, *N*=25), and (F,G) mean speed values of three biological replicates (*n*=3). Bars in graphs: median (D-F), mean (E–G). Statistical tests: ***$P \leq 0.001$, Dunn's multiple comparison (posthoc Kruskal-Wallis test) (D); ***$P \leq 0.001$, Dunnett's multiple comparison (posthoc ANOVA) (E–G).

Figure 3 – figure supplement 1

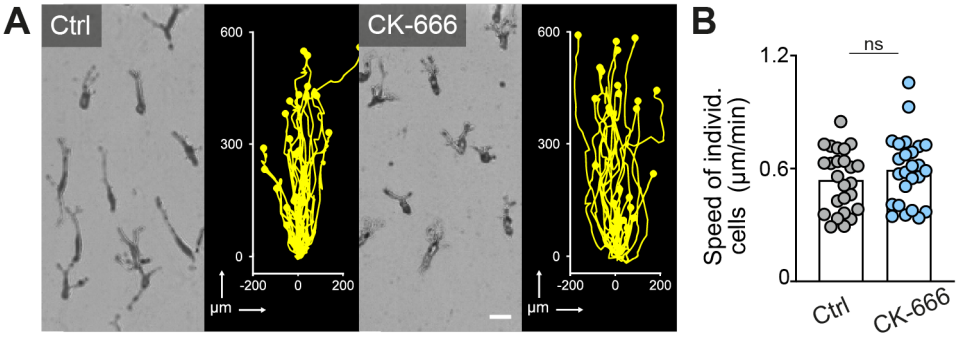

Figure 3 – figure supplement 1. Arp2/3 complex-mediated dendritic actin networks are dispensable for macrophage chemotaxis in 3D matrigel. (A) Representative cell morphologies (brightfield microscopy) and tracks over 24 h of BMDMs following a C5a gradient in matrigel in the presence of CK-666. Scale bar: 25 µm. **(B)** Analysis of BMDM chemotactic migration, individual cell speeds from one independent experiment (dots represent randomly chosen cells per condition, *N*=25). Bars display the mean; ns: non-significant, *t* test.

Figure 3 – figure supplement 2

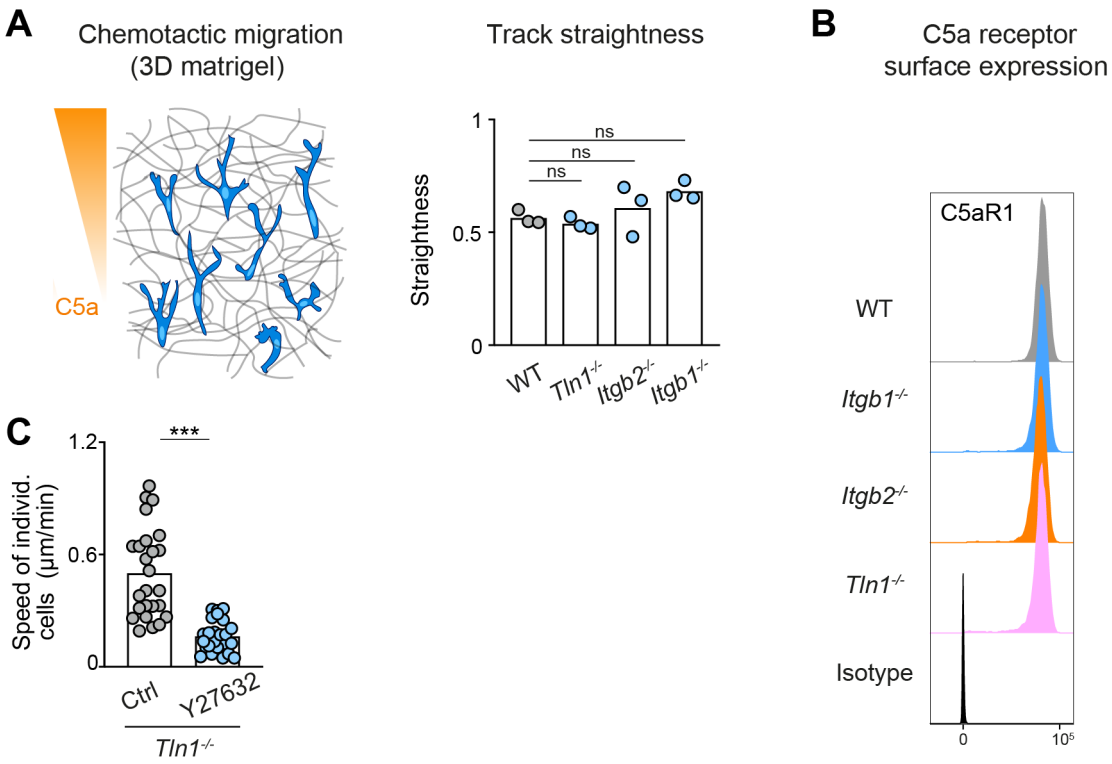

Figure 3 – figure supplement 2. Track straightness and C5aR1 expression are unaltered in chemotaxing BMDMs with impaired integrin functionality. (A) Analysis of track straightness during BMDM chemotactic migration toward C5a gradients. Mean speed values were calculated from three biological replicates (*n*=3). In each biological replicate *N*=25 cells were tracked and analyzed. Bars in graph display the mean; ns: non-significant, Dunnett's multiple comparison (posthoc ANOVA). **(B)** Flow cytometry analysis of C5aR1 cell surface expression on WT, *Itgb1*$^{-/-}$, *Itgb2*$^{-/-}$ and *Tln1*$^{-/-}$ BMDMs. C5aR1 acts as the major chemotactic receptor for the chemoattractant C5a. **(C)** Analysis of *Tln1*$^{-/-}$ BMDM chemotactic migration toward a C5a gradient in 3D matrigel in the presence of Y27632, individual cell speeds from one independent experiment (dots represent randomly chosen cells per condition, *N*=25). Bars display the mean; ***$P \leq 0.001$, *t* test.

Figure 4

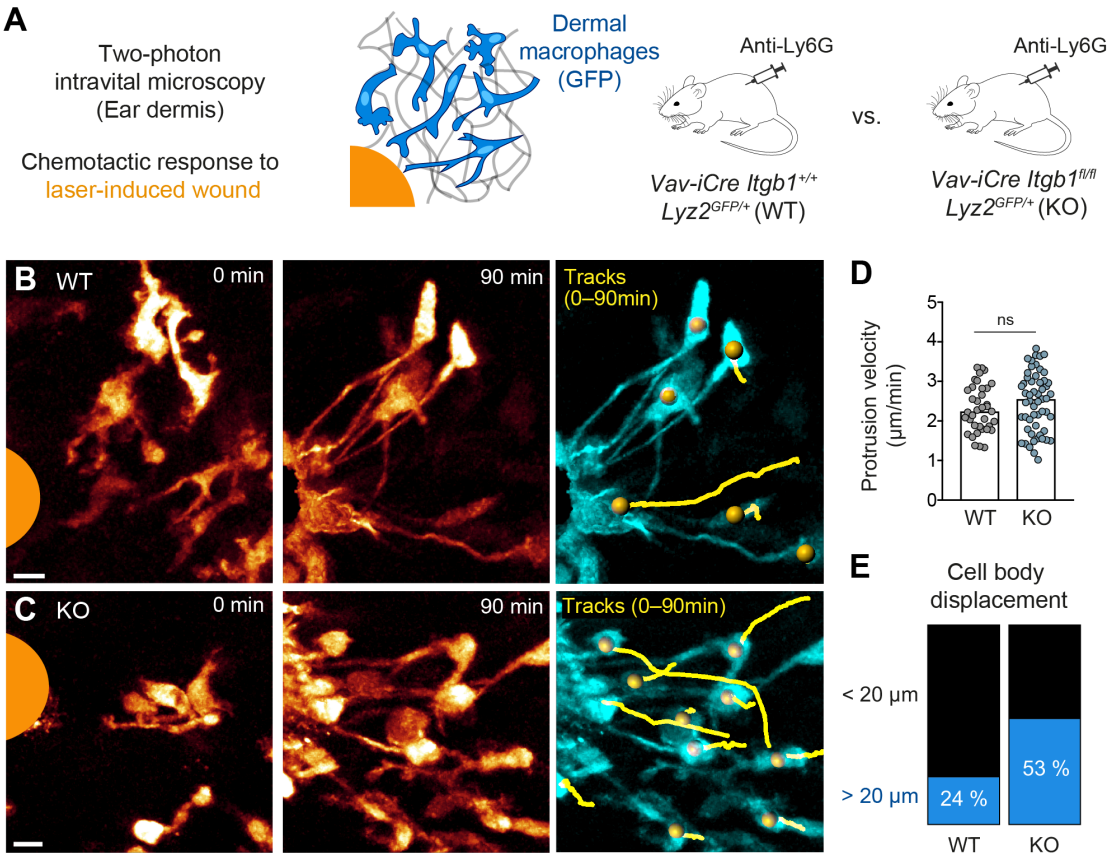

Figure 4. Amoeboid-like macrophages still perform chemotactic migration in mouse tissue. (A) Scheme for studying the chemotactic response of dermal macrophages to laser-induced tissue injury in mouse ear skin. Two-photon intravital microscopy (2P-IVM) was performed on *Vav-iCre Itgb1*$^{fl/fl}$ *Lyz2*$^{GFP/+}$ and littermate control mice. Mice were treated with Anti-Ly6G antibody to deplete neutrophils and avoid their presence in imaging field of views. **(B, C)** 2P-IVM images of GFP-expressing dermal macrophages in WT mice (B) and conditional *Itgb1*-deficient mice (C) at the onset of the wound response and 90 min later. GFP signal is displayed as glow heatmap color. Cell body displacements are shown as yellow tracks. Scale bars: 10 µm. **(D)** Velocity analysis of macrophage protrusions moving towards the tissue lesion. Each dot represents one protrusion (WT: *N*=37; KO: *N*=55). Values are pooled from *n*=3 (WT) and *n*=4 (KO) mice; ns: non-significant, *U* test. Bars are median. **(E)** Cell bodies of responding macrophages were tracked and categorized according to displacement (WT: *N*=34; KO: *N*=55). Values are pooled from *n*=3 (WT) and *n*=4 (KO) mice.

Figure 4 – figure supplement 1

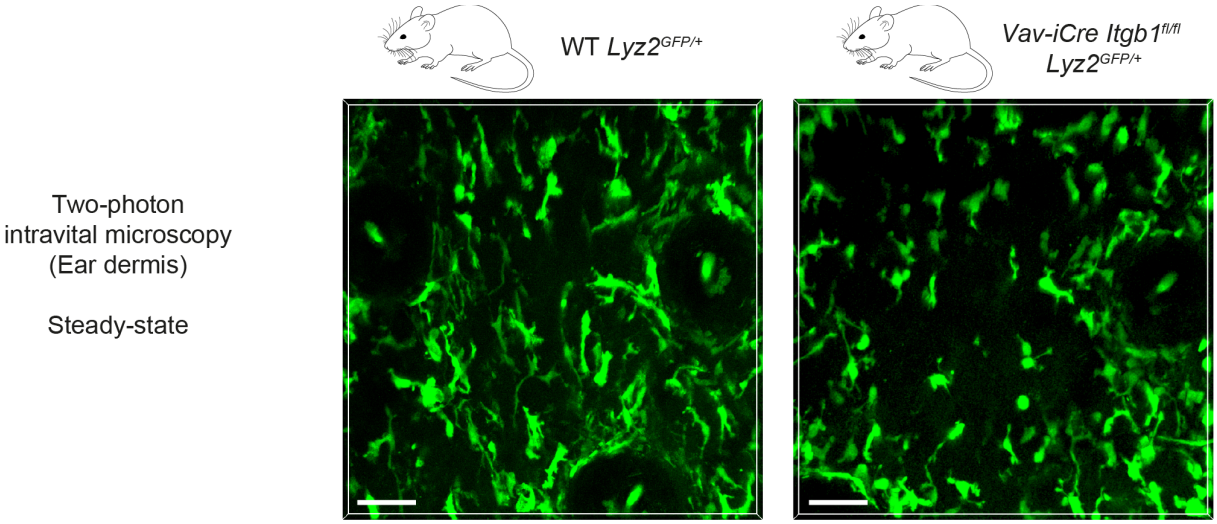

Figure 4 – figure supplement 1. Two-photon intravital microscopy of macrophage shapes in unchallenged mouse skin. Two-photon intravital microscopy of the dermal compartment in unchallenged ear skin reveals mesenchymal shapes with multiple elongated protrusions in GFP-positive macrophages of WT *Lyz2*$^{GFP/+}$ mice. In contrast, the majority of GFP-positive macrophages in the dermis of *Vav-iCre Itgb1*$^{fl/fl}$ *Lyz2*$^{GFP/+}$ mice showed more amoeboid-like morphologies and less pronounced cell protrusions. Scale bars: 50 µm.

Figure 4 – figure supplement 2

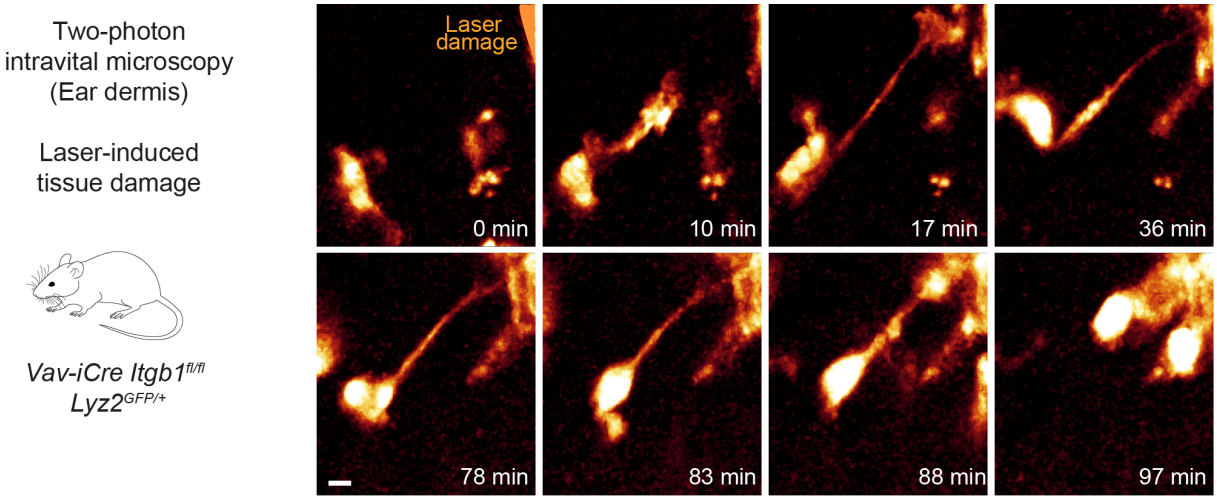

Figure 4 – figure supplement 2. *Itgb1*-deficient dermal macrophages perform chemotactic migration in mouse skin tissue. Close-up view and time sequence of an *Itgb1*-deficient macrophage that chemotactically responds to a laser-induced tissue lesion in the mouse dermis. Despite lack of β1 integrins and loss of mesenchymal cell shape, these cells form directed protrusions and displace their cell bodies toward the wound site. Scale bar: 5 µm.

Figure 5

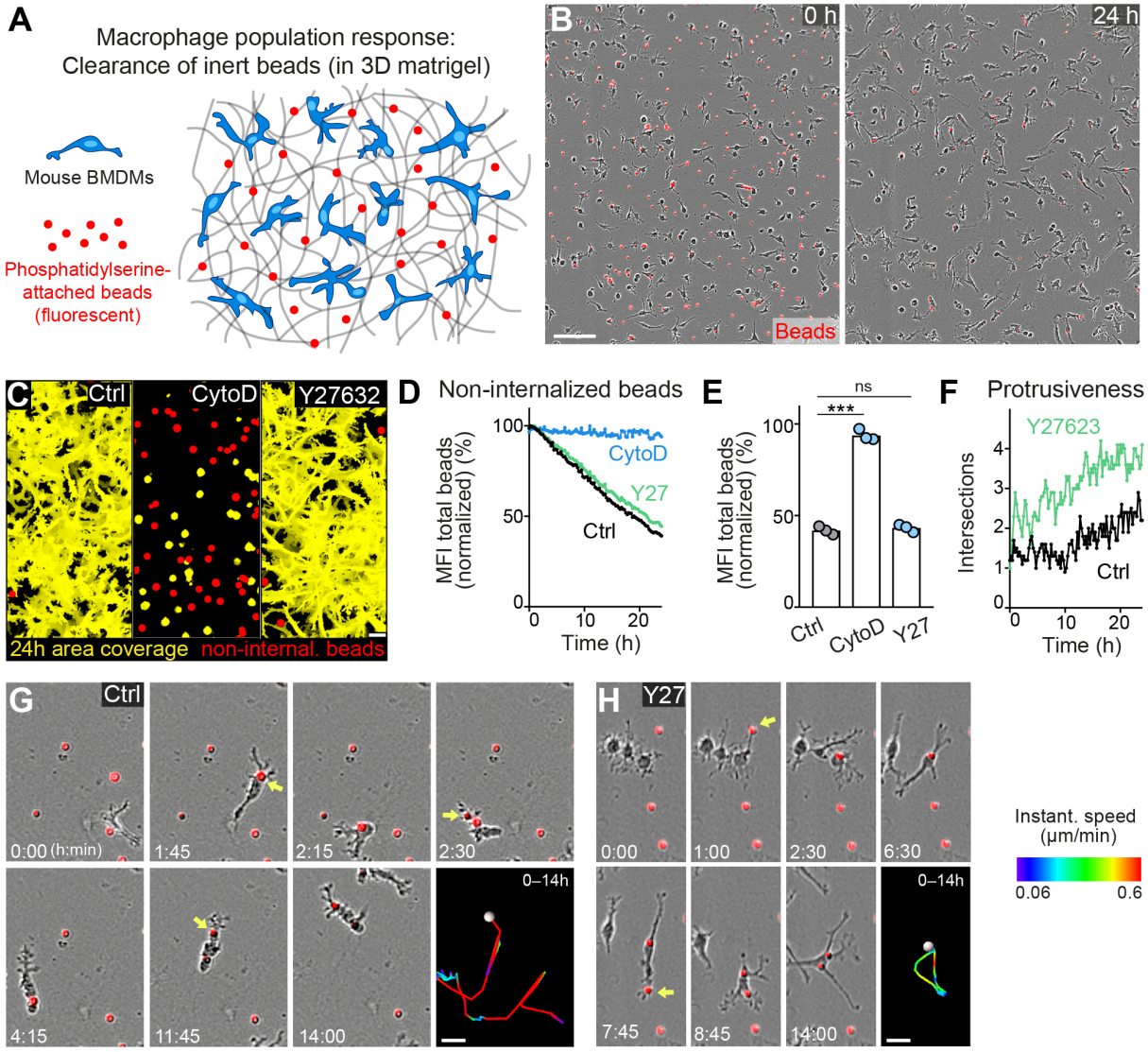

Figure 5. Movement and protrusiveness as two sampling strategies for bead removal by macrophage networks. (A) Scheme for studying macrophage network surveillance in 3D *in vitro* matrices. **(B)** Images of start (0 h) and endpoint (24 h) of bead removal by a population of WT BMDMs (unstained). Extracellular, fluorescent beads with surface-attached phosphatidylserine (red, 0 h) were ingested by BMDMs over time. The image shows a quarter of the total imaging field of view. **(C–E)** Analysis of BMDM network sampling activity in the presence of cytochalasin D (CytoD) or Y27632, including (C) time projections of macrophage shapes over 24 h, displayed as total area coverage (yellow) in relation to non-internalized beads (red). Bead sampling by macrophages was measured as mean fluorescence intensity (MFI) decline of bead fluorescence in 15-min intervals over time, presented as (D) time-course analysis from one independent experiment (dots in curves are mean values from N=4–5 technical replicates (separate wells of matrigel), and as (E) 24 h-mean-values calculated from three biological replicates (n=3 per genotype). **(F)** Cell protrusiveness of WT and Y27632-treated BMDMs was determined by Sholl analysis for N=10 randomly chosen cells and presented as mean values at 15-min time intervals over 24 h. **(G, H)** Time sequences of individual control (G) and Y27632-treated (Y27) (H) BMDMs, correlating bead sampling and migratory activity. Yellow arrows highlight bead uptake events. Cell tracks over 14 h are pseudo-colored for instantaneous speed values. All bar graphs display the mean; ***P≤0.001, ns: non-significant; Dunnett's multiple comparison (posthoc ANOVA). Scale bars: 100 µm (B), 40 µm (C), 20 µm (G, H).

Figure 5 – figure supplement 1

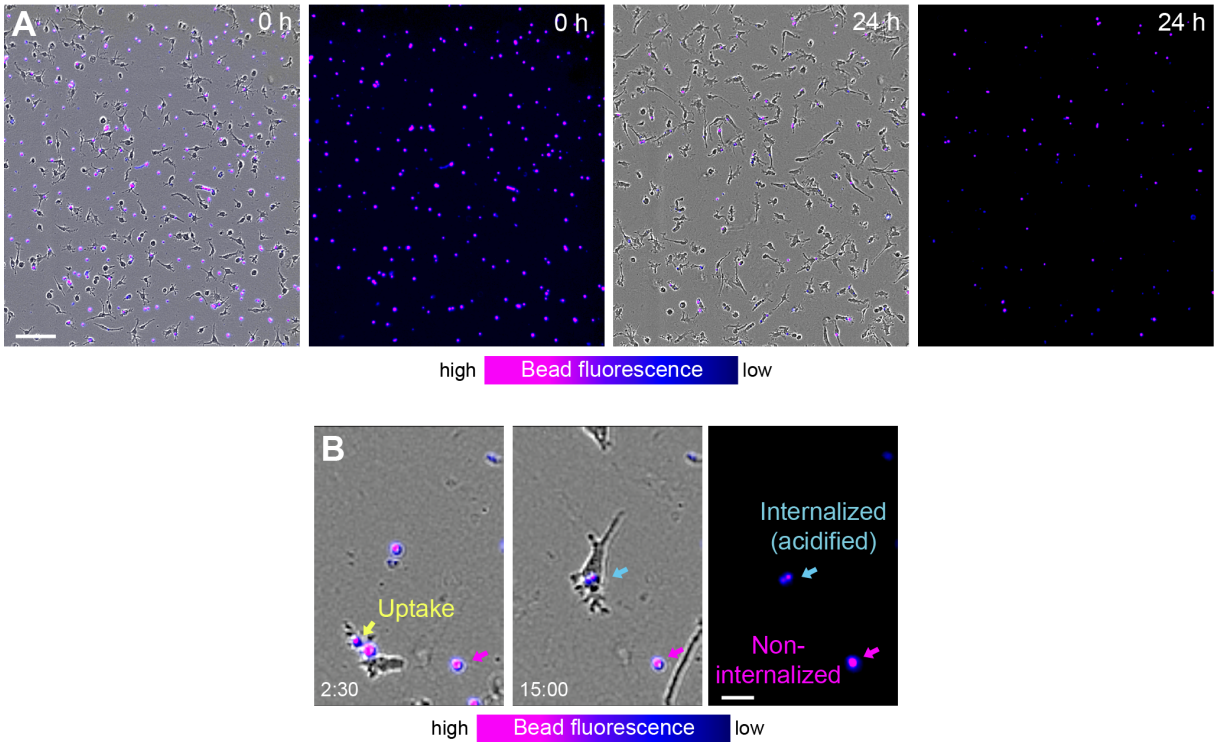

Figure 5 – figure supplement 1. Removal of fluorescent phosphatidylserine-attached beads by macrophage networks and individual macrophages. (A) Live cell imaging snapshots showing the start (0 h) and endpoint (24 h) of bead removal by a population of WT BMDMs (unstained). Fluorescent phosphatidylserine-attached beads were extracellular (red, 0 h) and fluorescence signal displayed as purple-blue heatmap color. At the onset of the experiment, most beads were extracellular and showed high fluorescence signal. After 24 h, the majority of beads was internalized by macrophages and showed low fluorescence signal. Scale bars: 100 µm. **(B)** Live cell imaging and close-up view of an individual WT BMDM that takes up a fluorescent bead at 2 h 30 min (yellow arrow). Approximately 12 hours later this internalized bead (light blue arrow) showed reduced signal due to fluorescence quenching in the acidic phagolysosomal compartment of the macrophage. In contrast, non-internalized beads (purple arrow) maintain the fluorescence signal over time. Scale bar: 20 µm**.**

Figure 5 – figure supplement 2

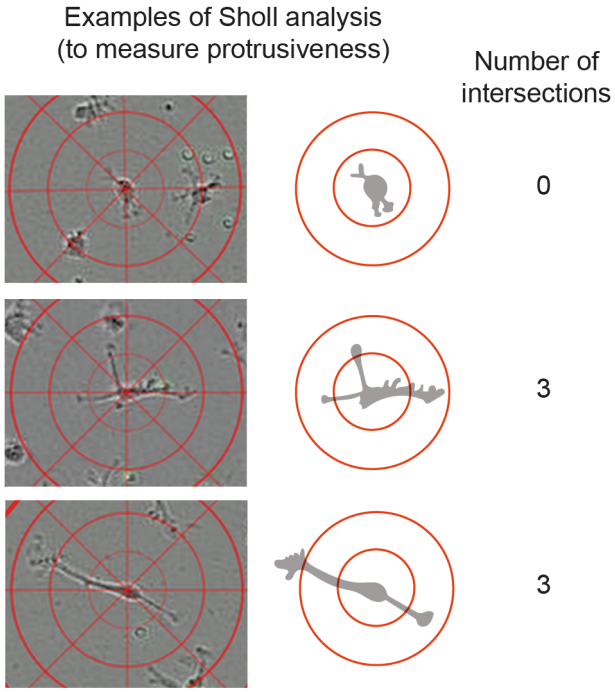

Figure 5 – figure supplement 2. Measurement of cell protrusiveness by Sholl analysis (relates to Figure 5F). The center points of individual macrophages are overlaid with layers of concentric rings (Sholl cells) at 25 µm intervals. The number of occasions Sholl shells are intersected by cellular process gives a measure of branch-based and elongation-based protrusiveness for an individual cell at a given timepoint.

Figure 6

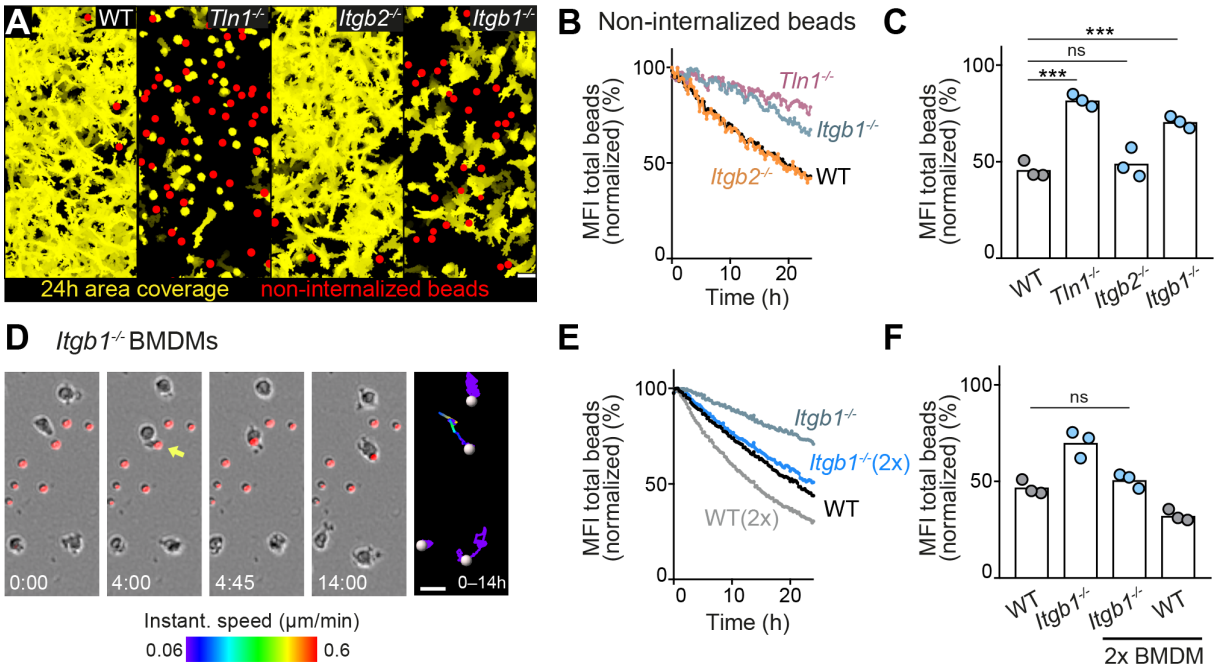

Figure 6. Haptokinesis is required for optimal bead removal by macrophage networks. (A–C) Analysis of BMDM network sampling activity upon genetic interference with integrin functionality was performed as described in Figure 5A–E. **(D)** Time sequence of an individual *Itgb1*$^{-/-}$ macrophage is shown, correlating bead sampling and migratory activity as described in Figure 5G and 5H. **(E, F)** Analysis of *Itgb1*$^{-/-}$ BMDM network sampling activity upon doubling (2x) the cell number in the BMDM network. Analysis of network sampling as described in Figure 5C–E. All bar graphs display the mean; ***$P \leq 0.001$, ns: non-significant; Dunnett's multiple comparison (posthoc ANOVA). Scale bars: 40 µm (A), 20 µm (D).

Figure 6 – figure supplement 1

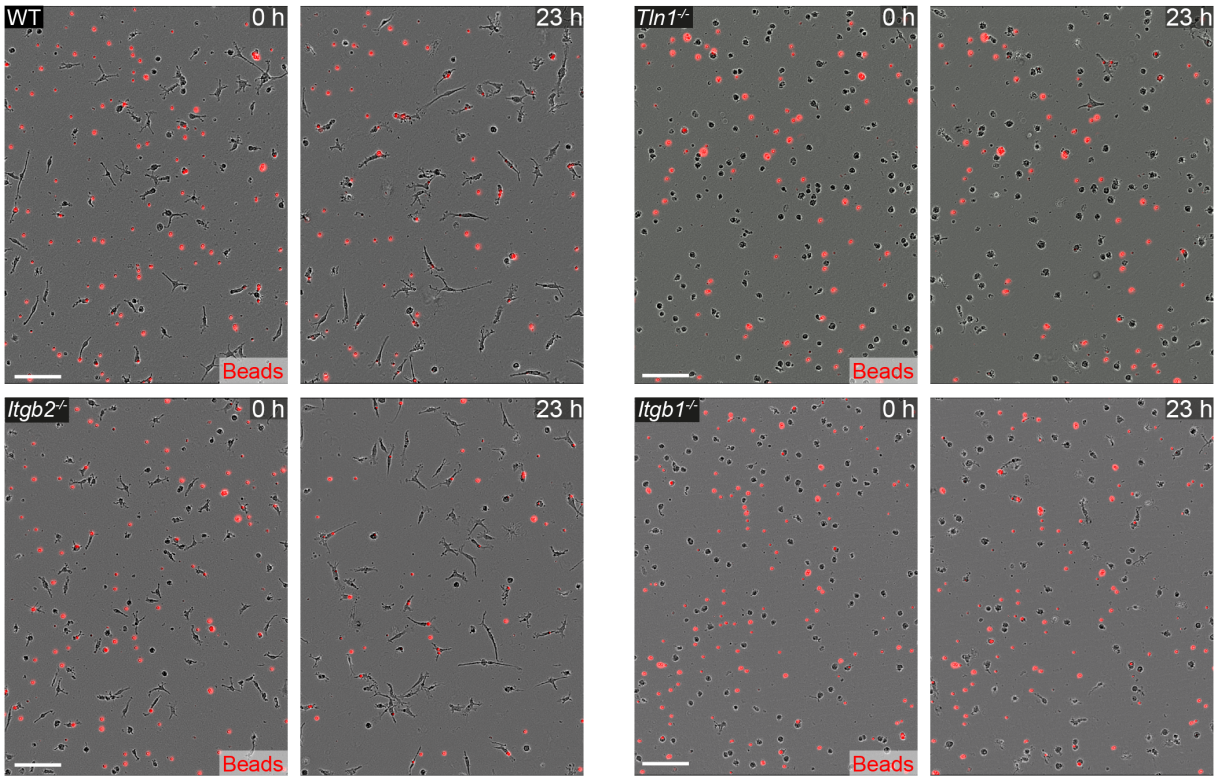

Figure 6 – figure supplement 1. Macrophages require β1 integrins for migration-dependent bead removal in 3D matrigel. Live cell imaging snapshots showing the start (0 h) and a late timepoint (23 h) of bead removal by populations of WT, *Itgb1*$^{-/-}$, *Itgb2*$^{-/-}$ and *Tln1*$^{-/-}$ BMDMs. WT and *Itgb2*$^{-/-}$ BMDMs move in 3D matrigel and reduce the number of extracellular beads, whereas migration-deficient *Tln1*$^{-/-}$ and *Itgb1*$^{-/-}$ BMDMs show impaired removal of extracellular beads. Extracellular, non-internalized fluorescent beads appear as bright red signal. Scale bars: 100 µm.

Figure 6 – figure supplement 2

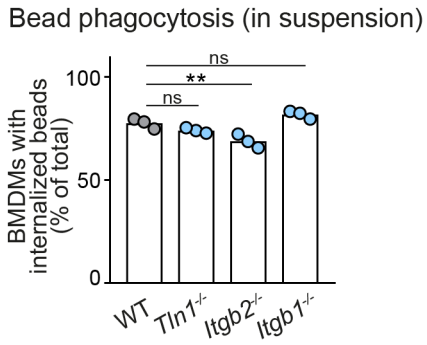

Figure 6 – figure supplement 2. Macrophages do not require β1 integrins bead phagocytosis in suspension. Analysis of bead phagocytosis in cell suspensions. WT, *Itgb1*$^{-/-}$, *Itgb2*$^{-/-}$ and *Tln1*$^{-/-}$ BMDMs were kept in stirred cell suspensions with fluorescent beads for a 2 h incubation time. Bead internalization by macrophages was quantified by flow cytometry analysis, using a combination of intrinsic bead fluorescence and an annexin V labelling of extracellular beads. Representative experiment with N=3 technical replicates. Bars display the mean; ns: non-significant, **P≤0.01, Dunnett's multiple comparison (posthoc ANOVA).

Figure 7

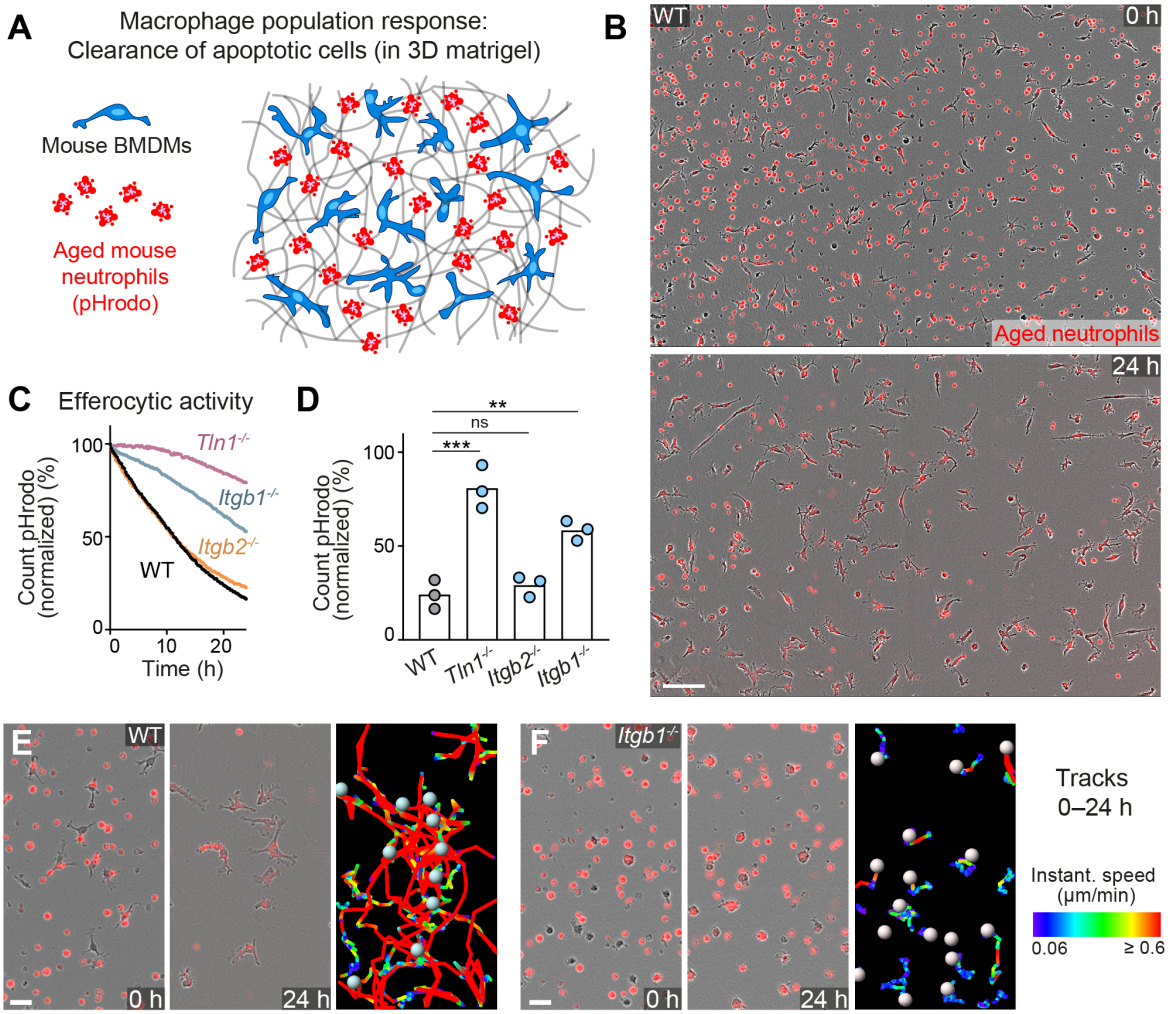

Figure 7. Haptokinesis is required for optimal efferocytosis by macrophage networks. (A) Scheme for studying the efferocytic response of macrophage networks in 3D *in vitro* matrices. **(B)** Live cell imaging snapshots showing the start (0 h) and endpoint (24 h) of dead cell clearance by a population of WT BMDMs (unstained). Extracellular, fluorescently pHrodo-labeled aged neutrophils (red, 0 h) were engulfed and removed by BMDMs over time. The image shows a quarter of the total imaging field of view. Scale bar: 100 µm. **(C, D)** Analysis of dead neutrophil removal by BMDM networks upon genetic interference with integrin functionality. Neutrophil uptake and digestion by macrophages was measured as an object count decline of pHrodo in 15-min intervals over time, presented as (C) time-course analysis from one independent experiment (dots in curves are mean values from N=2–5 technical replicates (separate wells of matrigel), and as (D) 24h-mean-values calculated from three biological replicates (n=3 per genotype). Bars display the mean; ***P≤0.001, **P≤0.01, ns: non-significant; Dunnett's multiple comparison (posthoc ANOVA). **(E, F)** Correlation of efferocytic and migratory activity in populations of WT (E) and *Itgb1*$^{-/-}$ (F) BMDMs. Cell tracks over 24 h are pseudo-colored for instantaneous speed values. Scale bars: 30 µm.

Figure 7 – figure supplement 1

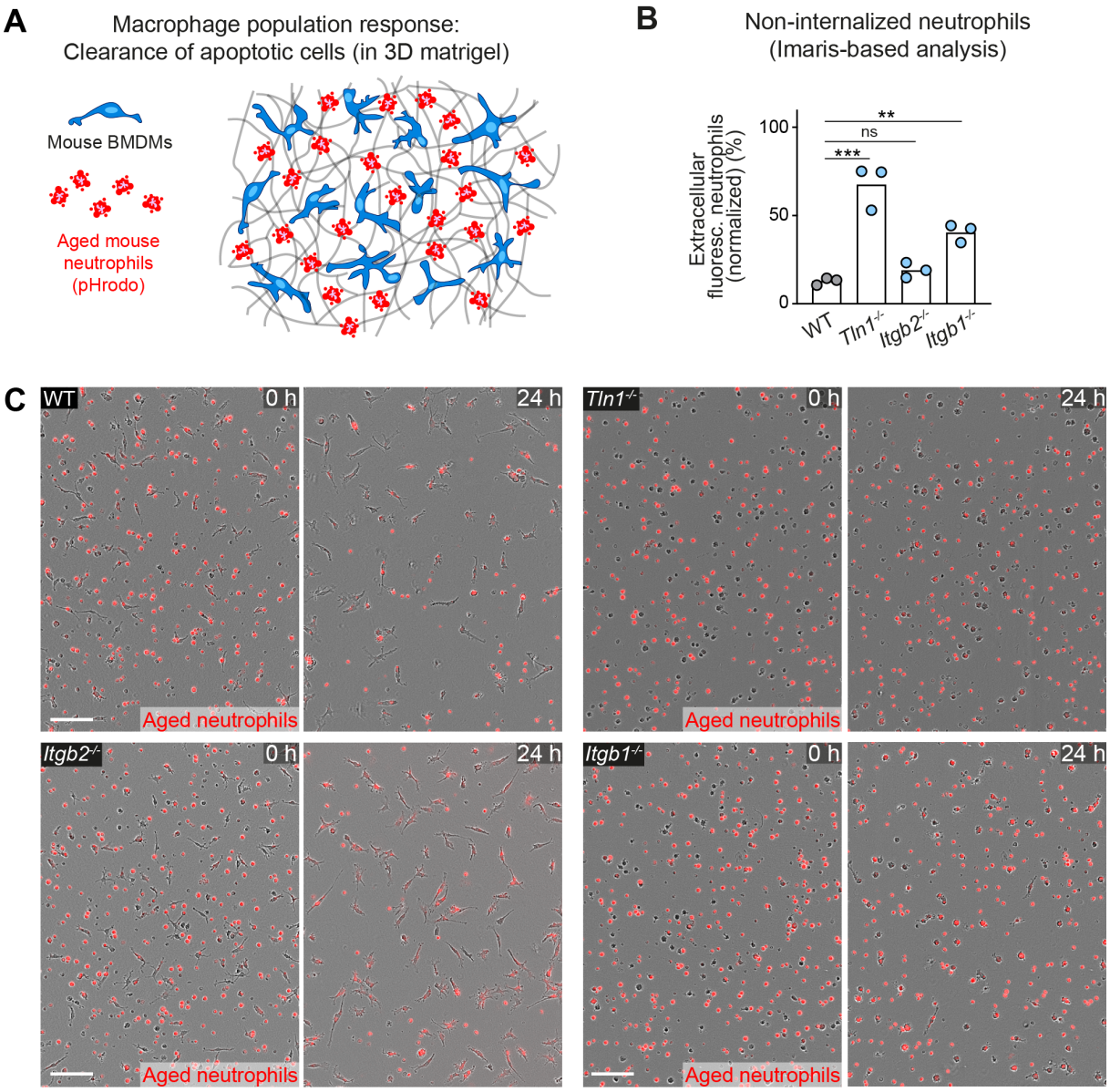

Figure 7 – figure supplement 1. Haptokinetic sampling of dead cells optimizes efferocytosis in macrophage networks. (A) Scheme for studying the efferocytic response of macrophage networks in 3D *in vitro* matrices (same as in Figure 7A). **(B)** Analysis of dead neutrophil removal after 24 h by BMDM networks upon genetic interference with integrin functionality. Validation of our analysis based on the integrated software of the Incucyte live cell imaging system (see Figure 7D). Imaris software-based analysis determined only the fluorescence signals of extracellular, non-internalized neutrophils 24 h after start of the experiment. Neutrophil uptake is measured as an object count and displayed as normalized values of the initial neutrophil numbers (0 h) for three independent experiments (N=2–5 technical replicates, which means imaging wells with BMDMs and matrigel). Bars are mean; ***P≤0.001, **P≤0.01, ns: non-significant; Dunnett's multiple comparison (posthoc ANOVA). **(C)** Live cell imaging snapshots showing the start (0 h) and endpoint (24 h) of dead neutrophil (red) removal by populations of WT, *Itgb1*$^{-/-}$, *Itgb2*$^{-/-}$ and *Tln1*$^{-/-}$ BMDMs. Non-internalized dead neutrophils show bright red signal. Scale bars: 100 µm.

Figure 7 – figure supplement 2

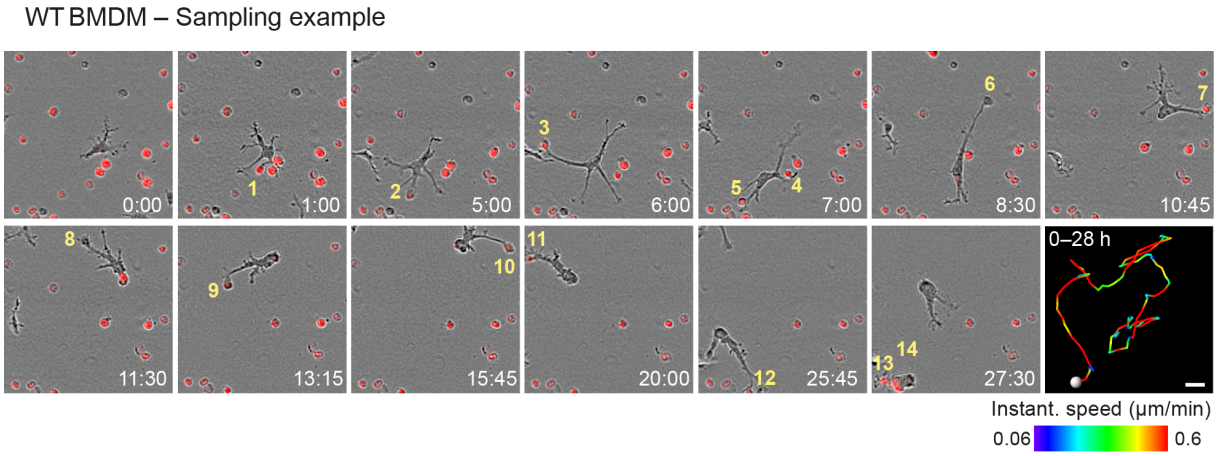

Figure 7 – figure supplement 2. Haptokinetic sampling of dead cells optimizes efferocytosis in macrophage networks. Live cell imaging and close-up view of an individual WT BMDM that samples and ingests several pHrodo Red-labeled dead neutrophils over 28 h. Yellow numbers indicate individual engulfed cell corpses. The cell track over 28 h is pseudo-colored for instantaneous speed values. Scale bar: 20 µm.

Figure 7 – figure supplement 3

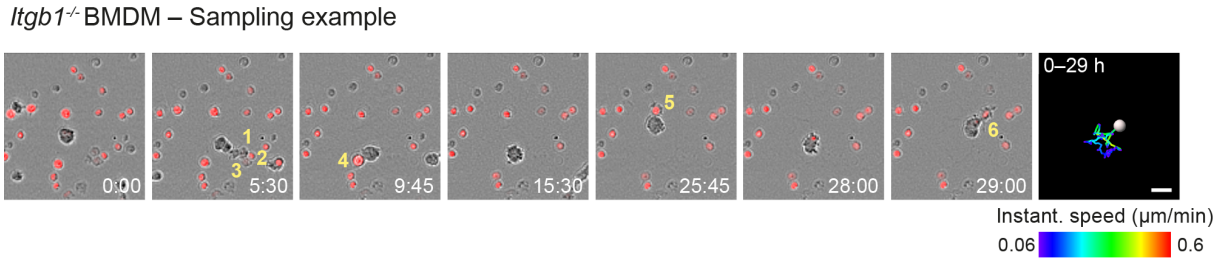

Figure 7 – figure supplement 3. Haptokinetic sampling of dead cells optimizes efferocytosis in macrophage networks. Live cell imaging and close-up view of an individual *Itgb1*$^{-/-}$ BMDM that samples and ingests several pHrodo Red-labeled dead neutrophils over 29 h. Yellow numbers indicate individual engulfed cell corpses. The cell track over 29 h is pseudo-colored for instantaneous speed values. Scale bar: 20 µm.

Figure 8

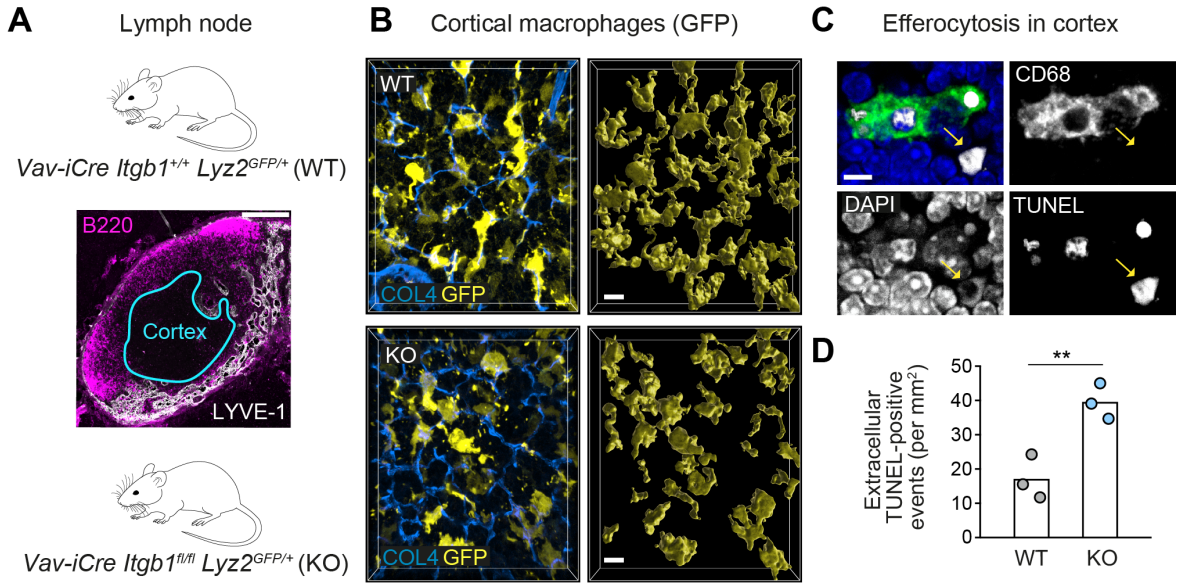

Figure 8. β1 integrin-dependent surveillance by cortical macrophage networks in lymph nodes. (A) Immunofluorescence staining of a mouse inguinal lymph node. T cell cortex (cyan outline) was defined as B220- and Lyve-1-negative tissue area. **(B)** Confocal immunofluorescence images of GFP-expressing cortical macrophages in WT and conditional *Itgb1*-deficient mice crossed to *Lyz2*$^{GFP/+}$ knock-in mice (left). Collagen IV (COL4) stainings display the cortical reticular fiber network. GFP-based surface representations of macrophage morphologies are shown (right). **(C)** Detection of apoptotic cells by TUNEL method in T cell zones of immuno-stained lymph node sections. TUNEL-positive cells had altered nuclear DAPI stainings, and were found non-internalized (yellow arrow) or internalized by macrophages (stained by CD68). **(D)** Quantification of non-internalized TUNEL-positive cells in T cell cortices. Dots represent individual mice (n=3 per genotype). Bars display the mean; **P≤0.01, t test. Scale bars: 100 µm (A), 10 µm (B), 5 µm (C).